Blackett Laboratory

Imperial College London, United Kingdom

MSci Physics Year in Europe

Project Report

Thore Mainart Bücking

2013

An Off-Axis Electron Gun for a Compact Electron Beam Ion Trap

This MSci thesis was completed by Thore Mainart Bücking at the Max-Planck-Institut für Kernphysik, Heidelberg under the supervision of

Priv. Doz. Dr. José R. Crespo López-Urrutia

Zusammenfassung:

Eine Elektronenstrahl-Ionenfalle (Electron Beam Ion Trap, EBIT), genannt *table-top* EBIT (*tt*EBIT), wurde im Rahmen dieser Arbeit fertiggestellt und in Betrieb genommen. Die *tt*EBIT benutzt Permanentmagnete, womit sie eine maximale Magnetfeldstärke von 0.7 T erreicht. Ihre geringe Größe erleichtert ihren Einsatz als diagnostisches Instrument in der Laserspektroskopie und bei Anwendungen mit Freie-Elektronen-Lasern und Synchrotron-strahlung.

Eine Halterung für eine Elektronenkanone, sowie ein Elektronenkollektor und andere Komponenten wurden entworfen und installiert. Somit konnte die Apparatur zum ersten mal in Betrieb genommen, und der Elektronenstrahl charakterisiert werden.

Darüber hinaus wurde eine neuartige "off-axis"-Elektronenkanone entwickelt, welche den externen Einschuss eines Photonenstrahles koaxial zum Elektronenstrahl erlaubt. Das Design wurde mit Simulationsprogrammen getestet und verspricht eine gute Kontrolle über die Strahleigenschaften. Dies wurde unter anderem durch sagittal und meridional Schnitte an den Elektroden erreicht, wodurch der Strahl in die gewünschte Richtung gesteuert werden kann.

Abstract:

An Electron Beam Ion Trap (EBIT) called *table-top* EBIT (*tt*EBIT) was completed and put into operation within the context of this work. The *tt*EBIT uses permanent magnets to produce a peak magnetic field of about 0.7 T. Its small size facilitates its use as a diagnostic tool in laser spectroscopy as well as its utilisation with free-electron lasers and synchrotronstrahlung.

A mounting for an electron gun, an electron collector, as well as other components were designed and installed. Thus the first commissioning of the apparatus and characterisation of the electron beam was achieved.

Furthermore, a novel off-axis electron gun was developed, which allows for a coaxial merging of a photon beam and the electron beam. The design was tested using simulation software and promises good control over the beam characteristics. This was achieved among other measures by placing sagittal and meridional cuts on the electrodes, which allows for the steering of the electron beam into the desired direction.

Contents

Introduction

The inception of the spectral analysis by Bunsen and Kirchhoff in the middle of the 19th century ushered in a new era in astrophysics and constitutes a milestone in experimental science. They discovered that elements emit light at various discrete wavelengths yielding well-defined characteristic spectra for each element, allowing them to identify the composition of various gas mixtures. A new, also very significant insight followed quickly: elements do not emit only at specific wavelengths, but they can also only absorb light of exactly the same wavelengths as well [1].

Thus, with the new tool called spectral analysis it was for the first time possible to analyse the constituents of our sun as well as other stars. This was done by looking at the bright emission lines of elements on earth and then comparing them to the dark (absorption) lines of an otherwise continuous emission spectrum of a celestial body. It was later discovered that the atoms in the corona of the Sun were actually present in highly ionised states [2] and it is now believed that a large fraction of the baryonic matter in the visible universe is in fact present in the form of such highly charged ions (HCIs) [3].

So, while HCIs are uncommon on earth, it can be understood that they play an important part in the study of stars, galaxies and other hot plasmas. One example of this is the role of iron (Fe) in the sun: while less than $0.1\,\%$ of its mass is Fe^{56+}, its large scattering cross section and the short lifetime of its excited states result in the fact that it causes a large fraction of all X-ray scatterings processes, making the sun a "wall of iron" from the photons' point of view. This in turn means that the "average photon" created in the centre of our Sun will take about 10 million years to reach its surface [4], reducing its energy output and ultimately allowing it to live for so long.

HCIs also appear in plasmas on earth: fusion reactors such as the Joint European Torus (JET) in the United Kingdom or the yet to be commissioned International Thermonuclear Experimental Reactor (ITER) in France are producing (or going to produce) plasmas that are so hot that they erode the plasma facing material (for example tungsten). Atoms from this erosion are then ionised due to the high temperatures and can have a strong effect on the overall efficiency of the reactor - just like in the sun. So, by knowing about the properties of HCIs, one gains further insight about the dynamics of fusion reactors.

But HCIs are not only important for plasma research: Many nuclear properties scale with the charge state (Z) of the atom, like the electron binding energy ($\propto Z^2$) and quantum electrodynamical (QED) effects ($\propto Z^4$). For example the Lamb-shift, i.e. the QED effect of an electron interacting with vacuum fluctuations, is for hydrogen in the region of a few μeV but grows to approximately $300\,eV$ when looking at U^{92+}, the heaviest stable element. Hence, it becomes possible to test QED theories to high accuracies and possibly even open a window to new physics beyond the standard model. One example of this is

the search for time dependence of the fine-structure constant α using the ion Ir^{17+} which has the highest reported α-variation sensitivity [5].

So it can be seen that HCIs play an important part in many active fields of research, which means that a systematic approach to their study is vital. To produce and study HCIs, the Electron Beam Ion Trap (EBIT) has proven to be an invaluable tool. It uses an electron beam, which is compressed to a few µm using a strong external magnetic field, yielding a high current density. Atoms are then sent through the beam where they are ionised due to collisions with the electrons. The positively charged ions are attracted by the negative space charge of the electron beam and hence are trapped radially. Another key feature of any EBIT are the so called drift tubes: cylindrical electrodes coaxial to the electron beam. By putting the drift tubes on different potentials the movement of the ions can be confined in the axial direction. The continuous exposure to the electron beam causes further ionisation until the outermost electron has a stronger binding energy than the electron beam's kinetic energy. The interactions with the electrons in the beam cause various light emitting processes, which can be analysed using a spectrometer.

While interactions with the electron beam already cause characteristic spectra, a laser can also be used for the targeted excitation (photo excitation) of the bound electrons. Since the photon energy can be very well defined, this resonant excitation or ionisation offers high accuracy, which can go to 10 ppm in the x-ray regime [6] and even below 1 ppm in the optical regime [7]. For measurements like this, the use of a high brilliance high flux laser like the free electron laser FLASH in Hamburg or the electron synchrotron BESSY II in Berlin is necessary. It is therefore very advantageous to have an EBIT which can be transported to the location of such lasers. Examples of this are the FLASH-EBIT [8] and HYPER-EBIT [9], which weigh several tons and are transported by truck and/or aircraft.

This work concerns the setting up and testing of the *table-top* EBIT (*tt*EBIT), i.e. an EBIT that uses permanent magnets to create the magnetic field and hence does not need cryogenic cooling, making much smaller than a regular sized EBIT. Because of the absence of cryogenic cooling the *tt*EBIT has also much lower building and maintenance costs and can be transported easily. The geometry of the drift tubes and magnet assembly was designed and assembled by L. F. Buchauer [10], whereas the electron gun, the electron collector and other important element of the *tt*EBIT will be discussed here.

Furthermore, an *off-axis* electron gun (OAG) was designed for the *tt*EBIT and shall be presented. This design leaves the beamline free of any obstructions, allowing for coaxial superposition of an external photon beam for photoionisation. Having the laser on the same axis as the electron beam is very advantageous because it maximises the fluorescence: while the trapping region is several mm across, it has only the diameter of the electron beam ($\approx 100\,\mu$m), which means that a non-parallel geometry would drastically reduce the overlap between the laser and the electron beam. Another advantage is the fact that the photon beam can be used at a second experiment behind the *tt*EBIT, which could be used to turn it into a diagnostic tool as well.

The OAG aims at high perveance, maximising the emitted current for a given extraction voltage. This is achieved by a unique design that was developed for this purpose. It also has a layout allowing for improved focusing capabilities, which was found to be vital for the functionality of the *tt*-EBIT by simulating the electron trajectories.

The theoretical details for the functionality of an EBIT will be discussed in chapter 1, covering the principles of an electron gun and the relevant processes inside the trap.

Because a significant amount of work is concerned with the simulation of the electron gun, the theory behind orbit integration will also be covered in this chapter. Chapter 2 describes parts that were designed for the tt-EBIT's first commissioning and chapter 3 discusses the produced electron beam. Chapter 4 describes the design process of the OAG and covers the layout of the gun. Chapter 5 summarises the work done and gives an outlook on the future of the ttEBIT.

Chapter 1

Theory

This chapter covers the relevant principles of an EBIT, starting with the important interactions inside the trap. Thereafter, the physics governing the key characteristics of the electron beam are described. Lastly, the theory of electron orbit simulation is discussed.

1.1 Electron-Ion Collisions

To produce ions, a typical EBIT uses an electron beam with a diameter of about $100\,\mu m$ [8] and a current between $0.02\,A$ and $5\,A$ [9]. By means of a classical approximation and assuming that an atom has a diameter of about $1\,\text{Å}$, it can be estimated that an atom is hit by an electron several million times a second. Inside such an electron beam, the injected atoms get ionised and trapped inside the beam forming a thin plasma. Ions in this plasma are trapped in the axial direction due to the electric potential of the drift tubes and radially because of the space charge of the electron beam (see fig. 1.1). Inside such thin plasmas it is only necessary to consider interactions between two particles at a time. A number of different interactions can take place. On the one hand there are the exciting or ionising processes, namely electron impact ionisation (EII), electron impact excitation (EIE), photoionisation (PI), and photoexcitation (PE). On the other hand there are the recombination processes: radiative recombination (RR) and dielectronic recombination (DR). All of these processes shall briefly be discussed in the following sections, to give an overview of the physics inside an EBIT.

There is also the possibility of ions colliding with atoms, which makes an electron exchange between them possible. This is a problem, because it slows the ionisation speed down if there is a constant influx of neutral atoms. Between ions, electron exchange becomes negligible because the electrostatic repulsion is stronger than the kinetic energy (E_{kin}) of the ions. While no electrons are exchanged during the collision process, the ions still exchange kinetic energy which means that they can thermalise.

The ion kinetic energy is also relevant for a another reason: if E_{kin} is higher than the trapping energy, the ions can leave the well and evaporate. The atoms enter the trap at room temperature, i.e. with an average energy of about $0.025\,eV$, the trapping potential however is usually around $Z \times 100\,eV$. Once inside the trap, the ions heat up through collisions with electrons and would thus evaporate quickly. An Fe^{24+} ion for example sees a potential barrier of $24e \times 100\,V = 2400\,eV$, which it can typically overcome within a
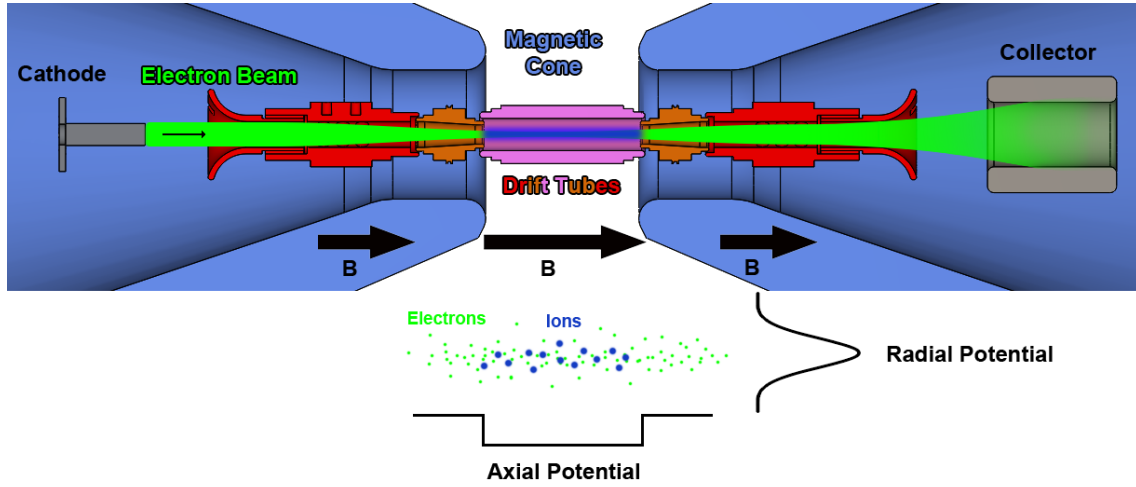
Figure 1.1: Schematic of the *tt*EBIT. The electron beam (green) ionises the atoms inside the trap (blue), where they are trapped axially because of the potential well of the drift tubes and radially because of the negative space charge of the electron beam.

second due to the collisional heating rate ($-e$ is the charge of an electron). So in order to achieve high charge states within a trap it is vital to produce them quickly, making a high current density crucial for the process. The trapping duration can be increased, using evaporative cooling. In this method, lighter ions are introduced into the system along with the ones being investigated (e.g. Ne and Ba). The Ne ions then see a lower potential barrier because their maximum charge state is lower than that of Ba (10 as opposed to 56), so they can evaporate quicker; this cools the ionic ensemble.

1.1.1   Excitation and Ionisation

The most important ionisation process is EII, which can take place if the electron beam energy is higher than the needed ionisation potential, or *binding* energy (E_b). Here the electron (e^-) collides with the ion of charge state Z (A^{Z+}) and gives a bound electron some if its kinetic energy, such that the bound electron can leave the ion:

$$A^{Z+} + e^-(E_{kin}) \rightarrow A^{(Z+1)+} + 2e^-. \tag{1.1}$$
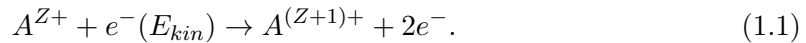
This process is visualised in fig. 1.2. As long as the ion is trapped, this process can take place until the highest possible charge state is reached (or in other words as long as $E_{kin} < E_b$). So by controlling E_{kin} the charge state of the ions can be controlled. To estimate the average time it takes for EII to take place, the cross section ($\sigma_{\text{EII}}(E_{kin}, A^{Z+})$) of the process needs to be known. The following semi-empirical formula by W. Lotz [11] is usually used estimate such cross sections (given that $E_{kin} > E_b$):

$$\sigma_{\text{EII}}(E_{kin}) = \sum_{n=1}^{N} a_n q_n \frac{\ln(E_{kin}/E_{b,n})}{E_{kin}E_{b,n}} \left[1 - b_n e^{-c_n(E_{kin}/E_{b,n}-1)} \right], \tag{1.2}$$
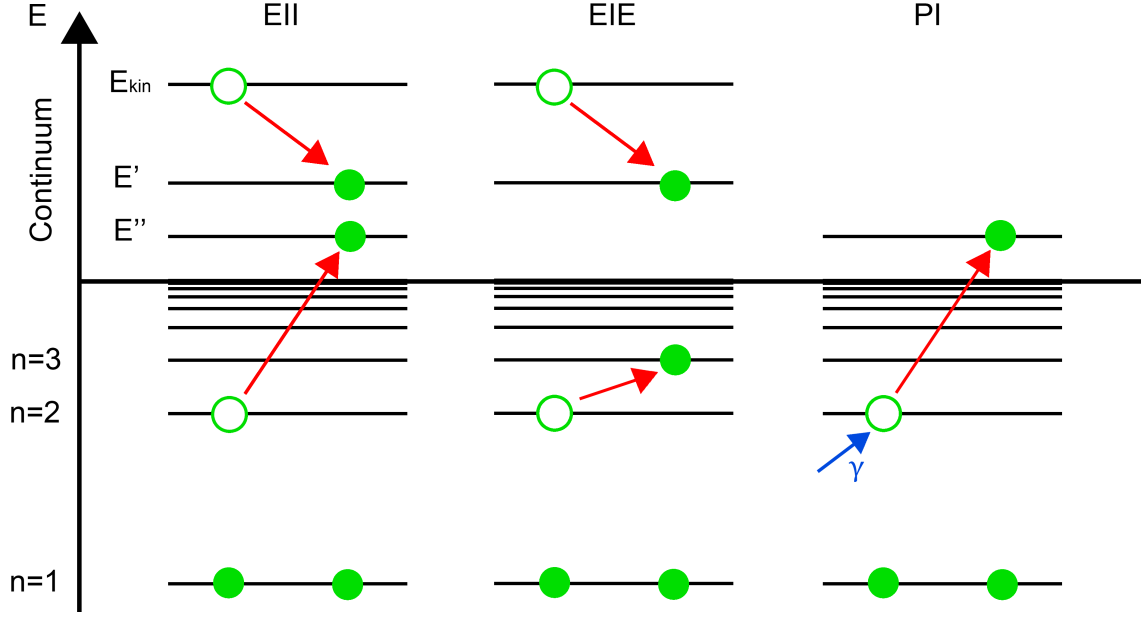
Figure 1.2: Energy diagram of electron impact ionisation (EII), electron impact excitation (EIE), and photoionisation (PI). The electrons in the beam have a kinetic energy E_{kin}, while the ion is in the ground state of an Li-like ion. The energy levels are not to scale.

where the sum is over all occupied principle quantum numbers (or *shells*) and q_n is the occupancy of that shell. E_b is here also dependent on n because each term of the sum depends on the binding energy of the corresponding shell. a_n, b_n, and c_n are fitting parameters that have to be found for each atom and charge state individually by experiment.

A typical plot of $\sigma_{\mathrm{EII}}(E_{kin})$ starts from zero at $E_{kin} = E_b$, peaks at around $E_{kin} \approx 3E_b$ and then gradually falls down with increasing E_{kin}. In fact, for $E_{kin} \gg E_b$ it can be shown that $\sigma_{\mathrm{EIE}} \propto \frac{ln(E_{kin})}{E_{kin}}$.

A process very similar to EII is EIE. Here the energy drop of the free electron (ΔE) is only enough to lift the bound electron to an excited state:

$$A^{Z+} + e^-(E_{kin}) \rightarrow (A^{Z+})^* + e^-(E_{kin} - \Delta E), \tag{1.3}$$
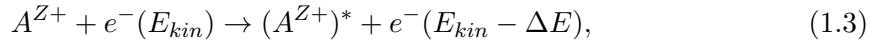
where $(A^{Z+})^*$ denotes an excited state. Note that E_{kin} can be lower than for EIE, because the energy gain of the bound electron is smaller. Another important difference is the fact that ΔE is quantised, i.e. the bound electron can only jump to well defined energy levels (see fig. 1.2).

Like EII, the cross section (σ_{EII}) is zero below the required minimum energy. The shape of the curve is dependent on the kind of transition (e.g. electric dipole transition) being looked at, but close to the maximum one can approximate [12]

$$\sigma_{\mathrm{EIE}} \propto \frac{1}{\Delta E}. \tag{1.4}$$

The excited state eventually drops to the ground state by emission of a photon with the energy

$$E_\gamma = \hbar\omega = \Delta E, \tag{1.5}$$

where $\hbar$ is the reduced Planck's constant and ω is the photon's angular frequency. This light can be spectroscopically analysed to gain information about the ion. EIE is a very important process for the analysis of plasmas because it is their the main channel for photon emission and the excitation is not limited by quantum mechanical selection rules one would otherwise encounter with PE [9].

PE and PI work in a similar way to EIE and EII, except that now a photon (γ) is interacting as opposed to an electron:

$$A^{Z+} + \gamma(\hbar\omega) \rightarrow \begin{cases} (A^{Z+})^* \\ A^{(Z+1)+} + e^- \end{cases}, \tag{1.6}$$
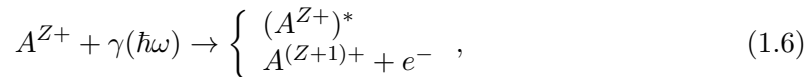
where the first equation is PE and the second one PI which can be seen fig. 1.2. Note that in PE and PI there is no emitted photon i.e. all its energy gets absorbed. This also means that PE is not possible if the photon energy is not exactly right. Therefore PE is ideal for spectroscopic analysis with an external laser: by tuning the frequency of the laser the different transitions can be individually targeted. A certain state is then excited if

$$\hbar\omega = E_{n'} - E_n, \tag{1.7}$$

where E_n and $E_{n'}$ are the energy levels of the ground state and the excited state respectively. The excited states would then decay, emitting a photon of the same wavelength in random directions, which can be detected.

1.1.2 Recombination

The time reversed version of PI is also possible:

$$A^{Z+} + e^- \rightarrow A^{(Z-1)+} + \gamma(\hbar\omega). \tag{1.8}$$
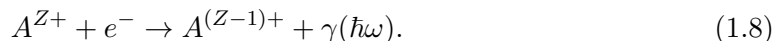
This process is called radiative recombination (RR) and can be seen in in fig. 1.3. Here, the free electron falls to an energy level $E_{n'}$, so that $\Delta E = E_{kin} - E_{n'} = \hbar\omega$. Its cross section ($\sigma_{\mathrm{RR}}$) is commonly significantly smaller than σ_{RII}, which makes the production of ions inside an EBIT possible [9]. However,

$$\sigma_{\mathrm{RR}} \propto Z^4, \tag{1.9}$$

which results in the fact that reaching higher charge states takes longer and longer, making a cooling system necessary.

There is also a resonant version of RR possible where the recombined electron lifts a bound electron to an excited state with $E_{n''}$ first before the ion falls back into the ground state emitting a photon, which is called dielectronic recombination:

$$A^{Z+} + e^-(E_{kin}) \rightarrow (A^{(Z-1)+})^* \rightarrow A^{(Z-1)+} + \gamma(\hbar\omega). \tag{1.10}$$
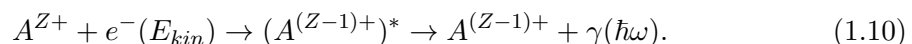
This process is only possible when $\Delta E = \hbar\omega$ (see fig. 1.3 for the special case $E_{n''} = E_{n'}$), so E_{kin} would have to be tuned such that the aforementioned condition is true. If so, the cross section of DR is three to five orders of magnitude larger than σ_{RR} [9], which makes this recombination process highly important for the analysis of plasmas.
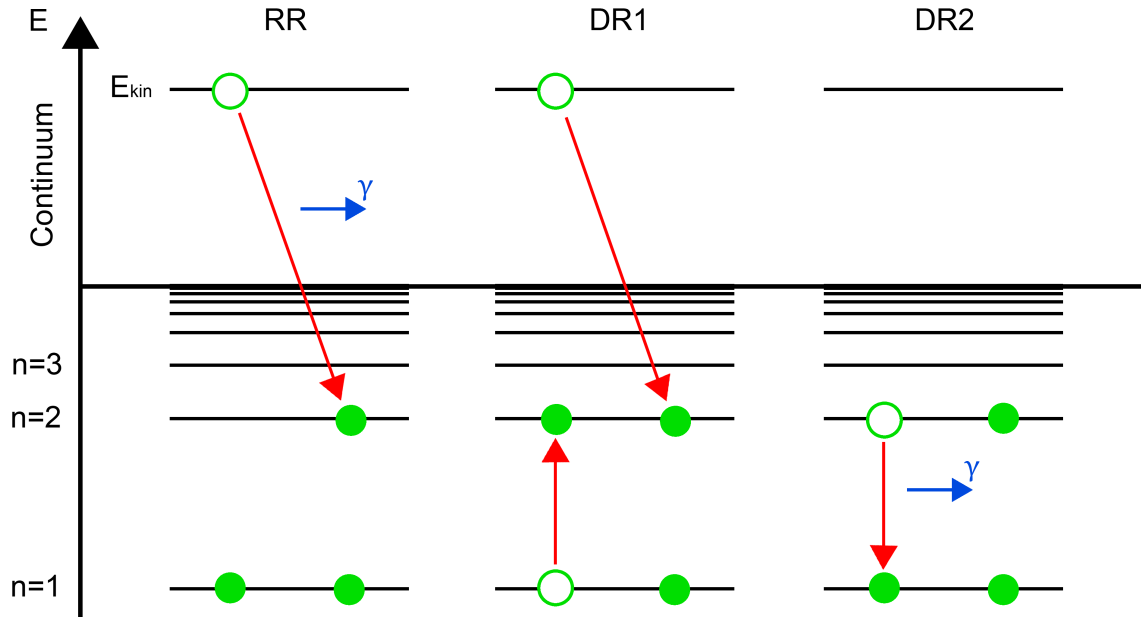
Figure 1.3: Energy diagram of resonant recombination (RR) and the two step process dielectronic recombination (DR). The electrons in the beam have a kinetic energy E_{kin}, while the ion is in the ground state of an Li-like ion. The energy levels are not to scale.

1.2 Electron Emission

An essential part of the EBIT is the electron gun. It produces the electron beam that is responsible for ionizing the atoms inside the trap and thus defines what charge states can be reached and how quickly the ionisation takes place. The concept of an electron gun is straightforward: electrons are emitted by a thermionic cathode and then accelerated (or extracted) through an anode with a hole in the middle. A third electrode, the focus, is positioned around the cathode in order to shape the beam and improve the homogeneity of the extracted current.

The extracted current (I) is limited by how many electrons the cathode can supply with the thermionic emission (source limited) and by the applied extraction voltage (space charge limited). Thermionic emission is based on heating the cathode up which increases the kinetic energy of the electrons inside the material. When the cathode is hot enough, the electrons have enough energy to overcome the potential barrier (or work function, W) between the cathode and the vacuum and can then leave the surface. We utilize a $\varnothing 3.4$ mm dispenser cathode with a porous tungsten matrix, impregnated with a mix of barium calcium aluminate from *Heatwave Labs* [13]. The Ba lowers the work function at the cathodes surface (to about 2 eV) to increase the maximum extracted current. Given that the cathode working temperature (T_c) of the cathode is around 1100 °C, the maximum electron output rate is found to be 0.5 A. Some Ba atoms are emitted along with the electrons, meaning that they have to be replenished at the cathodes surface via diffusion from a Ba reservoir between the heater and the tungsten matrix. Additionally, as long as the extracted current does not get close to 0.5 A, I can be considered space charge limited
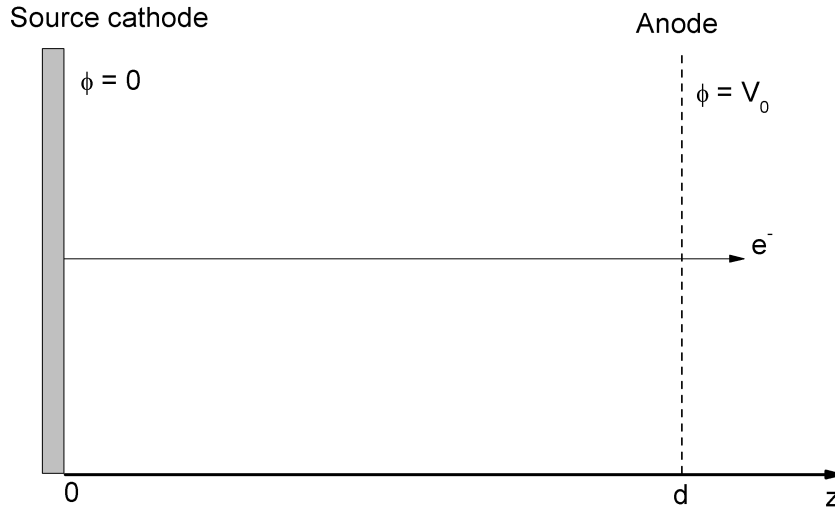
Figure 1.4: Geometry for calculation of space-charge-limit. The anode and cathode are considered to form a infinite planar gap of distance d.

(see 1.2.1). This is generally considered advantageous because it improves the uniformity of the emission [14, chapter 6.2].

   If the extraction voltage is high enough, the cathode emission is considered source limited, which means that the extracted current is now a function of T_c:

$$j = AT_c^2 e^{\frac{-(W-\Delta W)}{k_b T_c}} , \tag{1.11}$$

where j is the current density, A a constant, k_b the Boltzmann constant and

$$\Delta W = \sqrt{\frac{e^3 E_c}{4\pi\epsilon_0}}, \tag{1.12}$$

with e being the electrons charge, E_c the electric field at the cathode and ϵ_0 the vacuum permittivity [15]. So the current is then dependent on the cathodes temperature as well as the extraction voltage.

1.2.1   Space Charge Limit

The space charge limit is an important factor for the electron gun design and shall be derived here for the one-dimensional case. For the non-relativistic electrons, this can be done by considering a continuous particle flow between infinite planar sheets of distance
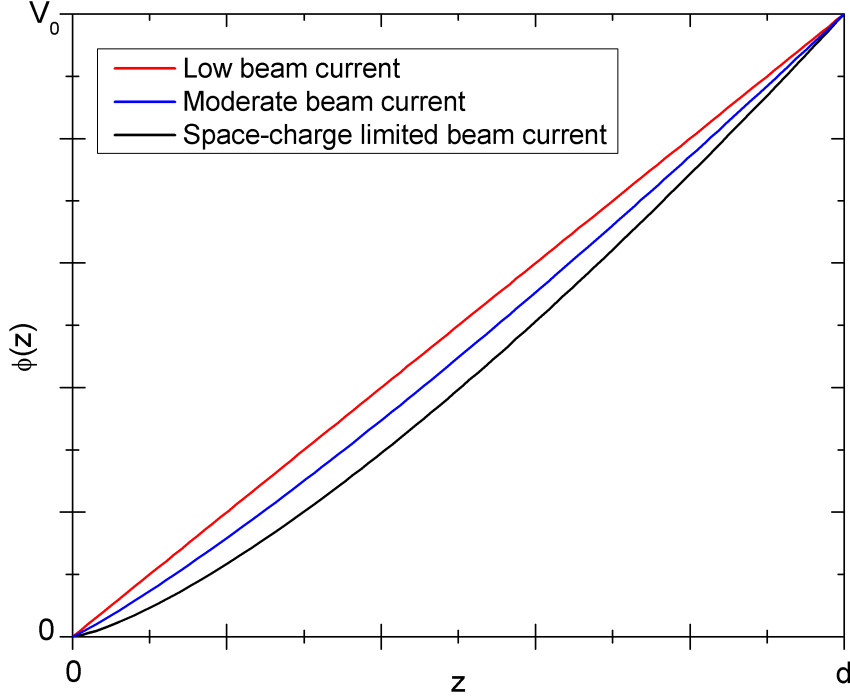
Figure 1.5: Electrostatic potential ϕ in an infinite planar acceleration gap of distance d and voltage V_0.

d with a voltage V_0 (see fig. 1.4). The particle velocity (v) and the electric potential (ϕ) are then related by

$$\frac{1}{2}m_e v(z)^2 = e\phi(z),\qquad(1.13)$$

where m_e is the electron mass and the boundary condition $v(0) = 0$ was used. Assuming a constant current, this can be used to obtain

$$\rho(z) = j\sqrt{\frac{m_e}{2e\phi(z)}},\qquad(1.14)$$

where ρ is the charge density and the relation $j = \rho \times v$ was used (v being the electrons velocity). I.e. this is expressing the beam density as a function of ϕ. Now, for self-consistent space-charge fields, the Poisson equation for electric fields needs to be fulfilled, which is

$$\nabla^2\phi = -\frac{\rho}{\epsilon},\qquad(1.15)$$

where $\epsilon = \epsilon_r\epsilon_0$ is the permittivity. Substituting eq. 1.14 into eq. 1.15 and using the correct boundary conditions yields Child's law for space-charge-limited extraction:
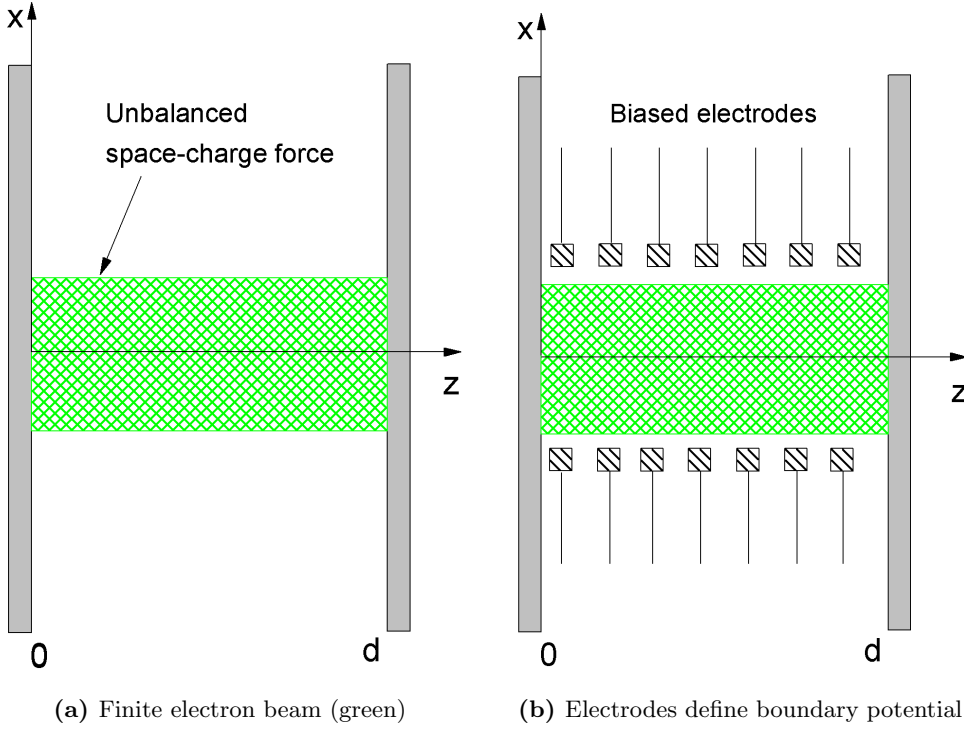
(a) Finite electron beam (green)   **(b)** Electrodes define boundary potential

Figure 1.6: Geometrical basis for the Pierce design. The electron beam has a finite extent in the x-direction, which would distort the beam envelope.

$$j = \frac{4\epsilon}{9} \sqrt{\frac{2e}{m_e}} \frac{V_0^{\frac{3}{2}}}{d^2}. \tag{1.16}$$

The right boundary conditions are $\phi(0) = 0$, $\phi(d) = V_0$, and $\frac{d\phi(0)}{dz} = 0$. The last one can be understood when considering the electric field: the space charge of the beam is stronger near the cathode, because the electrons are slower and hence more densely packed. The higher the extracted current, the stronger the space charge effect, the more the electrical potential is pushed down near the anode (see fig. 1.5). If the space charge gets too strong, the electric field at the cathode approaches zero and the electrons are not able to leave anymore. The black curve in fig. 1.5 is simply described by

$$\phi(z) = V_0 (\frac{z}{d})^{\frac{4}{3}}, \tag{1.17}$$

which is derived from eq. 1.16 combined with eq. 1.15. The derivation of Child's law assumes that the cathode is an infinite planar mesh and is therefore not always valid; it does however give a good approximation for many ion and electron sources [14, chapter 5.2].
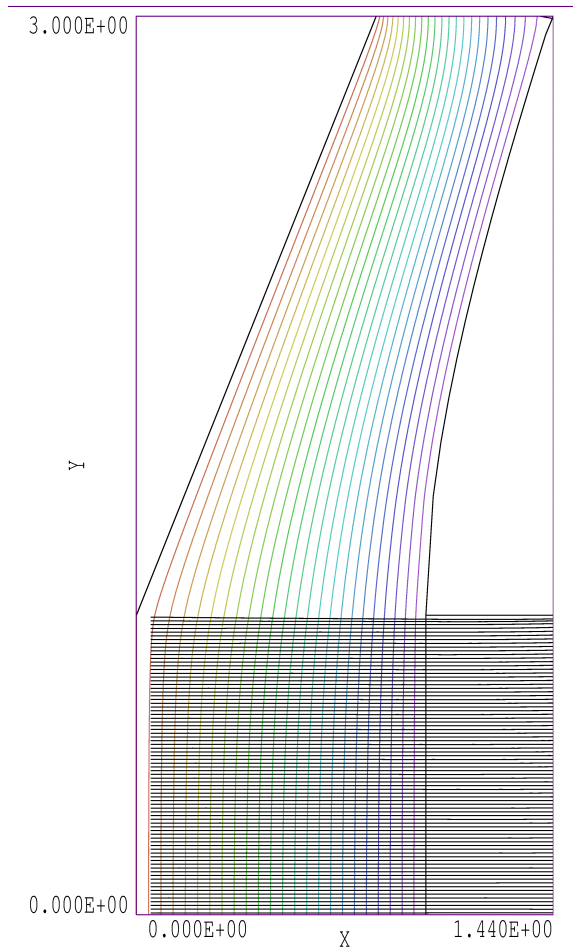
Figure 1.7: Demonstration of the Pierce design using the software package TriComp. The simulation assumes infinite extension into the plane, the equipotential lines (in colours) are equally spaced between $0\,\mathrm{kV}$ and $50\,\mathrm{kV}$ and the units on the x and y-axis are in inch. The black lines show the simulated electron trajectories, which start on the left at $x = 0$ and propagate to the right.

1.2.2 Pierce Geometry

The self-consistent solution for a non-relativistic two-dimensional electron (or ion) gun was derived by J. R. Pierce in 1949 and follows the same geometrical assumptions as in 1.2.1, except that now the current is supposed to take up a finite area (see fig. 1.6).

Now, while the electrons in the infinite sheet beam see a potential behaving according to eq. 1.17, the electrons at the edge in fig. 1.6a would diverge away from the z-axis. It can be seen that by placing biased electrodes along the edge and putting them on potentials according to eq. 1.17, this problem would be solved. A more practical extension of this approach is to shape the electrodes such that this boundary condition is fulfilled. It was shown in [16] that this means that the cathode and the anode have to follow

$$\frac{4}{3}\theta = \frac{\pi}{2} \quad \text{and} \quad (\frac{r}{d})^{\frac{4}{3}}\cos(\frac{4\theta}{3}) = 1 \tag{1.18}$$

respectively, where θ and r are defined by the functions $z = r\cos\theta$ and $x = r\sin\theta$. This can be seen in fig. 1.7, where the upper half of the plane is pictured.

1.2.3   Electron Guns for EBITs

The previous considerations assumed a mesh as the anode, so that the beam could pass through, but for higher power guns this mesh would quickly melt. It is therefore necessary to develop a geometry suitable for an anode with an aperture. If this aperture is big in comparison to d, the beam would defocus, which is why the condition

$$d \geq D_a, \tag{1.19}$$

with D_a as the diameter of the aperture has to be imposed. The maximum extracted current could then be estimated using eq. 1.16:

$$I = j \times A \approx \left[\frac{4\epsilon}{9} \sqrt{\frac{2e}{m_e}} \frac{\pi D_a^2}{4d^2} \right] V_0^{\frac{3}{2}} \approx 2 \times 10^{-6} V_0^{\frac{3}{2}}, \tag{1.20}$$

where A is the extraction area. With a limit like this it is useful to define the quantity *perveance*,

$$P = \frac{I}{V_0^{\frac{3}{2}}}. \tag{1.21}$$

P can be increased by focusing the beam so that a smaller aperture can be used. Also the space charge is lower at the cathode than it would have been for a non-converging design. There is no analytical solution for the maximisation of P, but beam imperfections limit P to roughly 3 µperv [17].

To increase j further, EBITs use a magnetic field in the axial direction to compress the electron beam. The compression can be understood when looking a single electron moving with a velocity v perpendicular to a magnetic field $\boldsymbol{B}$. Defining $\boldsymbol{B}$ to point into the z-direction ($\boldsymbol{B} = B_z \equiv B$), the electron will then rotate around the z-axis with the radius of gyration r_g and an angular frequency (the *Larmor* frequency) given by

$$\omega_l = \frac{eB}{2m_e}, \tag{1.22}$$

where e and m_e are the charge and mass of the electron respectively. Due to conservation of angular momentum it can be seen that with increasing B, r_g will decrease. The dynamics of an electron beam inside a magnetic field was first discussed by G. Herrmann [18], who was considering a thermionically emitting cathode, i.e. with electron velocities following the Maxwell-Boltzmann distribution. Furthermore, the space charge of the beam was also taken into account. He showed that the beam can be described in terms of the Herrmann radius r_0

$$r_0 = r_B \sqrt{\frac{1}{2} + \sqrt{\frac{1}{4} + \frac{8m_e k_B T_c r_c^2}{e^2 B^2 r_B^4} + \frac{B_c^2 r_c^4}{B^2 r_B^4}}}, \tag{1.23}$$

where r_c is the radius of the cathode and B_c the magnetic field at the cathode. r_B is the Brillouin radius defined by

$$r_B = \sqrt{\frac{m_e I}{\pi \epsilon_0 v_z e B^2}}, \tag{1.24}$$
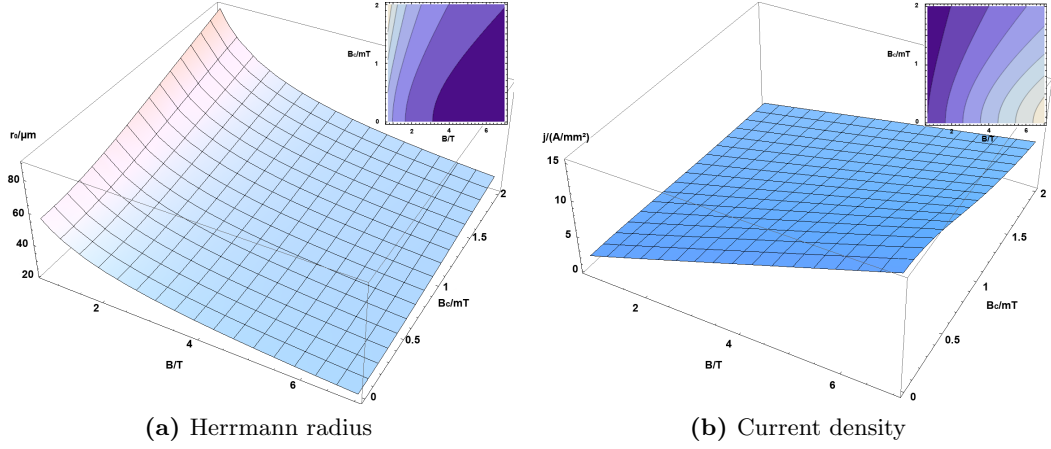
(a) Herrmann radius

(b) Current density

Figure 1.8: Plots of the Herrmann radius (1.8a) an the resulting current density (1.8b). The variables were chosen as follows: $T_c = 1100\,°C$, $r_c = 1.7\,mm$, $I = 20\,mA$, $v_z = 3 \times 10^6\,m\,s^{-1}$.

where v_z is the velocity in the z direction. r_0 defines a circular section of the beam in the xy-plane that contains about $80\,\%$ of the electrons in that plane, so now $j = j(z, r)$. In general it is desirable to keep r_0 as low as possible at the trap centre, because that means a higher current density. For the magnetic field this means that B has to be as high as possible while keeping B_c as low as possible. Reducing the cathode temperature however, is not a viable solution in most cases because the cathode needs to be hot enough to supply the desired current. In fact, the advantage of more thermionic emission in general outweighs the larger Herrmann radius, when looking at the current density.

The effect of changing B and B_c can be seen in fig. 1.8 over a range of $B = [0.7, 7]T$, which corresponds to the magnetic field strengths at the trap centre of the *tt*EBIT at the lower limit and the HYPER-EBIT at the higher limit [9]. It can be seen that j increases nearly linearly at these magnitudes of B, but there is a strong impact if there is a slight change in B_c. Denoting j_{tt} and j_{HYPER} as the current densities for $B = 0.7\,T$ and $B = 7\,T$ the impact of the lower magnetic field can be described as the fraction $\frac{j_{tt}}{j_{HYPER}}$, which is pictured in fig. 1.9 for variable B_c. Given an expected value of $B_c \approx 1\,mT$, it can be seen that the *tt*EBITs current density will be roughly $12\,\%$ of the HYPER-EBITs, assuming they have the same B_c. For stronger B_c in the *tt*EBIT, j drops to about $10\,\%$.

The charge state of an ion can be controlled by choosing the electron energy inside the trap, which is given by

$$E_e = e(\phi_{DT} - \phi_{cat} - \phi_{sc}),\qquad(1.25)$$

where ϕ_{DT}, ϕ_{cat}, and ϕ_{sc} are the potentials of the drift tube, the cathode, and the space charge effect respectively. ϕ_{DT} and ϕ_{ca} can be independently defined, whereas ϕ_{sc} can be found using eq. 1.15, which gives

$$\phi_{sc}(r \leq r_0) = \frac{I}{4\pi\epsilon v_z}\left[\left(\frac{r}{r_0}\right)^2 + \ln\left(\frac{r_0}{r_{DT}}\right)^2 - 1\right]\qquad(1.26)$$
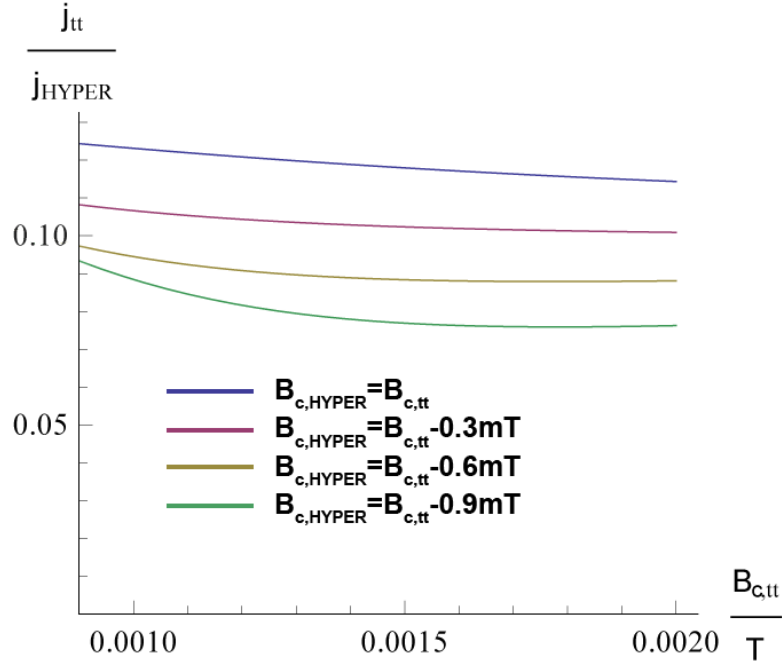
Figure 1.9: Effect of the weaker magnetic field strength in the centre of the ttEBIT in comparison to the HYPER-EBIT. The different curves simulate a stronger B_c in the ttEBIT, because it does not have the same magnetic shielding.
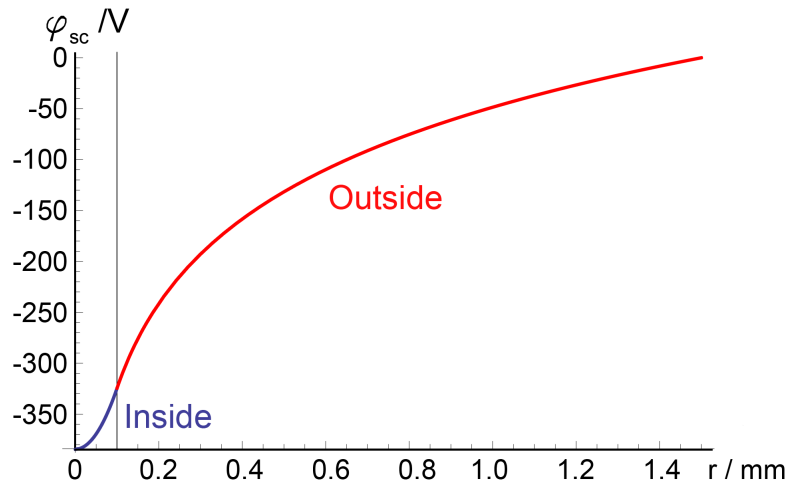

Figure 1.10: Predicted space charge potential as a function of r with a beam radius of $0.1\,\mathrm{mm}$, $r_{DT} = 1.5\,\mathrm{mm}$, $v_z = 3 \times 10^6\,\mathrm{m\,s^{-1}}$, $I = 20\,\mathrm{mA}$, and $\phi_{DT} = 0\,\mathrm{V}$. 'Inside' and 'Outside' denote the regions inside and outside of the electron beam respectively.

(a) TriComp   **(b)** SIMION
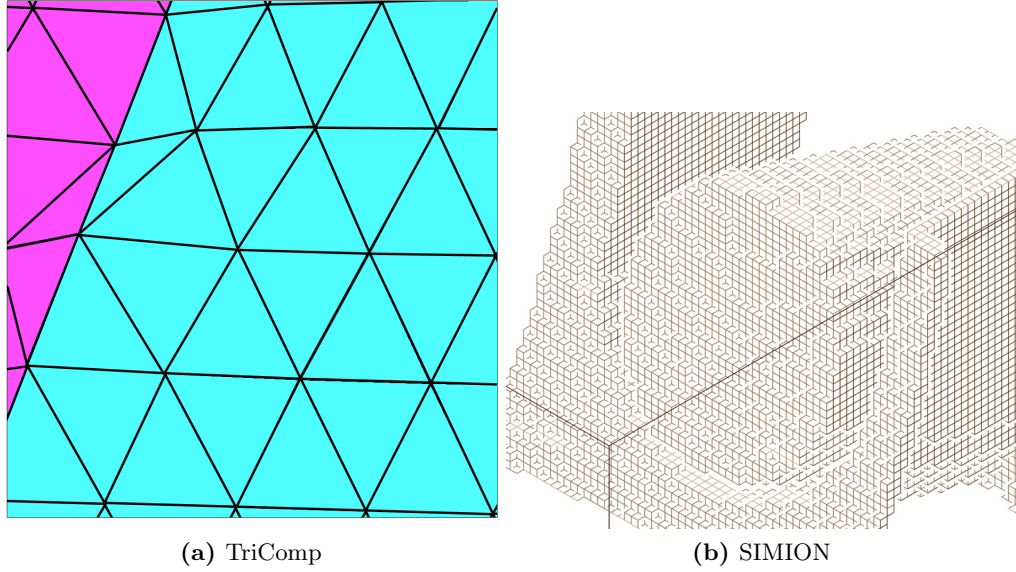
Figure 1.11: Illustration of voxels: (a) Mesh created by TriComp. The geometry is part of
fig. 1.7, with the pink region being an electrode and the blue region being vacuum. It can be seen
how the triangles are skewed to fit to the border of the regions. (b) Geometry in SIMION. The
small brown boxes are electrode voxels, while the vacuum is see-through.

and

$$\phi_{sc}(r \geq r_0) = \frac{I}{4\pi\epsilon v_z} \ln\left(\frac{r}{r_{DT}}\right)^2 \tag{1.27}$$

which is approximating the electron beam to have a with homogeneous charge density
between $r = 0$ and $r = r_0$, no space charge for $r > r_0$, and $\phi_{DT} = 0\,\text{V}$ [19]. r_{DT} is the
drift tubes' inner radius. ϕ_{sc} is negative in general and responsible for trapping the ions
radially (see fig. 1.10). It can be seen from eq. 1.26 that decreasing r_0, as well as increasing
I, increases the trapping depth.

1.3   Trajectory Simulations

To calculate the path of an electron (the *orbit*) in a more complex situation, simulation
software is essential. Electron beam simulations were performed using the software pack-
ages TriComp and SIMION 8.0, both of which are based on the finite element method, i.e.
approximating the electric and magnetic field to be constant in a small volume of space.
These volumes (*voxels*) can then either be treated as a dielectric with permittivity $\epsilon = \epsilon_r \epsilon_0$
and charge density ρ or as an electrode with a potential ϕ. After having calculated the
electric and magnetic fields, the electron orbits can then be calculated by advancing it in
small time steps, which will be explained in more detail in this chapter.

The TriComp software uses a 2D geometry which can applied to axially symmetric
problems by appropriate geometric transformations. It turns a 2D sketch into a mesh of
small triangles by moving the corners of the triangles onto the pre defined boundaries of
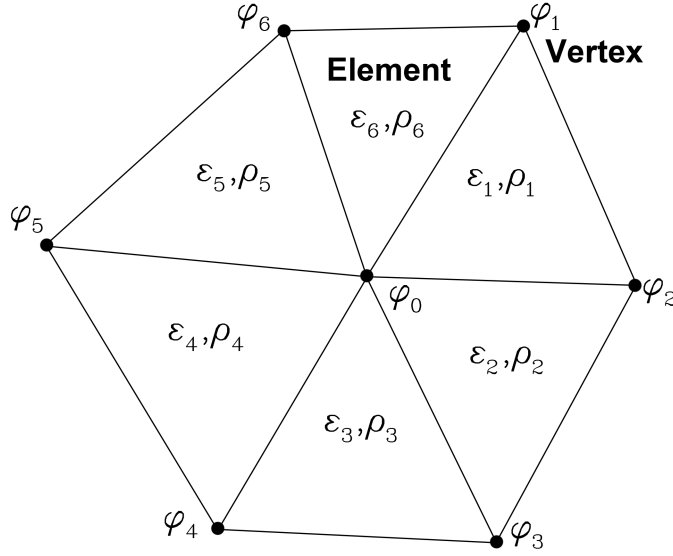the physical object one is interested in (see fig. 1.11a). These triangles are then revolved

Figure 1.12: Elements surrounding a vertex point. Each element i has a constant ϵ_i and ρ_i while ϕ is only defined at the vertex points.

around the z-axis forming rings with cylindrical symmetry, each with a constant electric and magnetic field ($\boldsymbol{E}$ and $\boldsymbol{B}$ respectively).

SIMION on the other hand uses cubic voxels, which grants the possibility of using a geometry without any symmetries, but has the downside that the boundaries of the voxel cannot be adjusted to the desired objects. So, to achieve a realistic accuracy the voxels need to be fairly small (see fig. 1.11b), which is more demanding on the computer's memory than the 2D approach and makes the simulation slow.

Since the simulation is concerned with steady state solutions, the relevant equations for $\boldsymbol{E}$ and $\boldsymbol{B}$ are Gauss's law,

$$\oiint_S \boldsymbol{E} \cdot d\boldsymbol{S} = \iiint_V \frac{\rho}{\epsilon} dV \tag{1.28}$$

and Ampère's law,

$$\oint \boldsymbol{B} \cdot d\boldsymbol{l} = \mu \iint_S \boldsymbol{j} \cdot d\boldsymbol{S}, \tag{1.29}$$

where $\mu = \mu_r \mu_0$ is the permeability. The limits are over a closed surface and the volume enclosed by that surface for Gauss's law and over a closed loop and the area enclosed by that loop for Ampère's law. Here, the electrostatic solution to a 2D mesh shall be considered using triangular pixels (or *elements*), whereas a full derivation of the finite element method can be found in [20]. Such a triangular element is then taken to be the smallest unit of division, so no finer information about the region can be gained. This means that inside one element ϵ and ρ are taken to be constant and the electrostatic potential ϕ is only relevant at the mesh vertices, i.e. the corners of the elements (see fig. 1.12).

With these assumptions a 2D version of Gauss's law can then be rewritten for each vertex as

$$\phi_0 \sum_{i=1}^{6} W_i - \sum_{i=1}^{6} \phi_i W_i = \sum_{i=1}^{6} \frac{\phi_i A_i}{3\epsilon_0}, \tag{1.30}$$

where A_i is the area of element i and W_i is a coupling constant depending on the shape of the elements i and $i+1$ as well as their ϵ (see [20, chapter 2.7]). This results in a large set of coupled equations that can be solved on a computer.

Inside an electromagnetic field the motion of an electron can be described using the Lorentz force:

$$\boldsymbol{F} = e(\boldsymbol{E} + \boldsymbol{v} \times \boldsymbol{B}), \tag{1.31}$$

where $\boldsymbol{v}$ is the velocity of the electron. By advancing the orbit in small time steps (Δt) it can always be checked in which element the electron is in and adjust the force acting on it accordingly. This simulation is only valid for very low currents though, because the space charge of the beam is not included. For self-consistent beam-generated electric fields, TriComp assigns a total current I, which is consistent with the space charge limited emission described in 1.2.1. Each particle is then carrying a fraction of the current ΔI, making each particle representing a group of electrons. So for each time step a particle is inside an element, that element gains a charge $\Delta I \Delta t$ which changes the electric field in and around that element. As this changes the trajectory of the individual orbits, several iterations have to be done until the solution converges (see [21]).

Chapter 2

The *table top* EBIT

This chapter explains the design of various components of the new table top electron beam ion trap (*tt*EBIT) and addresses key issues relevant for their functionality. The *tt*EBIT uses strong permanent magnets instead of a superconducting electromagnet, making the entire apparatus a fraction of the size of a common EBIT and thus allowing for easy transport and low costs. The vacuum chamber, magnetic system and the drift tubes (DTs) were designed and assembled by L. F. Buchauer [10], leaving the electron gun, collector, electrical setup and gas injection system to be constructed. For first commissioning, the *tt*EBIT was assembled using an already existing on-axis electron gun which will be introduced here. The behaviour the guns electron beam was predicted using TriComp and compared to measurements.

2.1   Overview

An overview of the *tt*EBIT can be seen in fig. 2.1 and shows four main functional parts: the electron gun (yellow), the drift tubes (purple), the magnetic system (blue and green) and the collector (brown). The magnetic system, drift tubes, and the main chamber are described in detail in [10], whereas the collector and electron gun shall be described in ch. 2.3 and ch. 2.2.

The device operates in an ultra-high vacuum ($< 10^{-7}$ mbar) and has external dimensions of $32 \, \text{cm} \times 30 \, \text{cm} \times 30 \, \text{cm}$. The magnetic system is based on 48 neodymium magnets (green) and a soft iron/magnetic steel construction (blue) that guides the field towards the trap centre, leading to a peak magnetic field of about $0.7 \, \text{T}$ (see fig. 2.2). Inside the pole pieces, which are shaped as hollow cones sits the vacuum chamber (grey), which holds the drift tubes and provides access to the trap centre with four radial ports. It also has room in the axial direction, where the electron gun and the collector are positioned.

The electron gun is held in place using a manipulator needed for adjustments. Also on that side of the *tt*EBIT are the high voltage connections for the electron gun.

The drift tube assembly consists of five electrodes which are named DT1-5 from the electron gun's side to the collector's side and are held in place with top-hat shaped mountings (holders)(see fig. 2.3). Their overall length is $108 \, \text{mm}$ and they have a minimum diameter of $3 \, \text{mm}$. Their electrical connections use one of the four radial access ports of the central cube and attach to feedthrough connectors on the rim of the connecting flange,
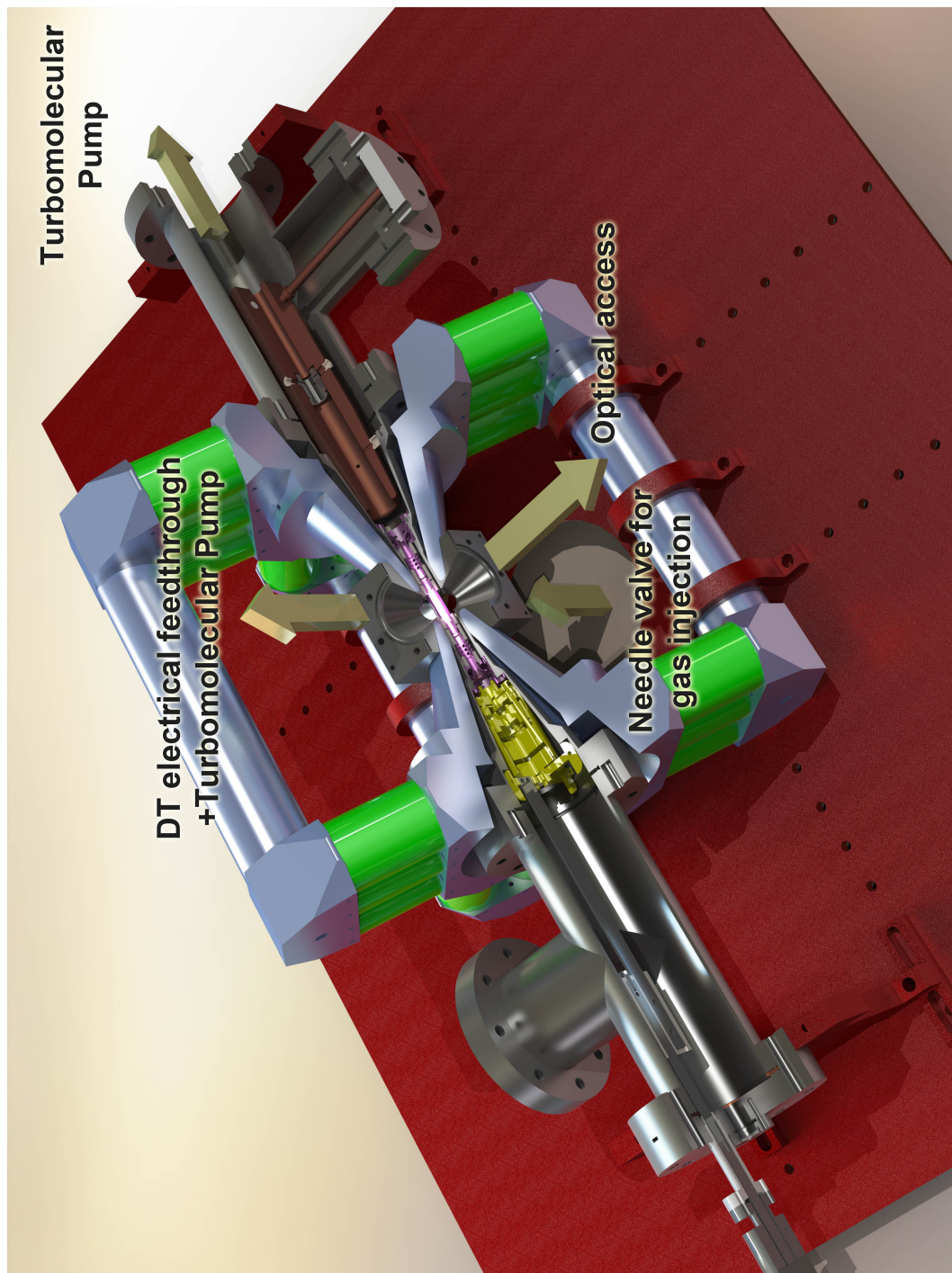
Figure 2.1: Overview of the *tt*EBIT. The electron gun (yellow) sits in front of the drift tubes (purple), behind which is the collector (brown). The magnetic system is blue with green magnets and the vacuum construction is grey.
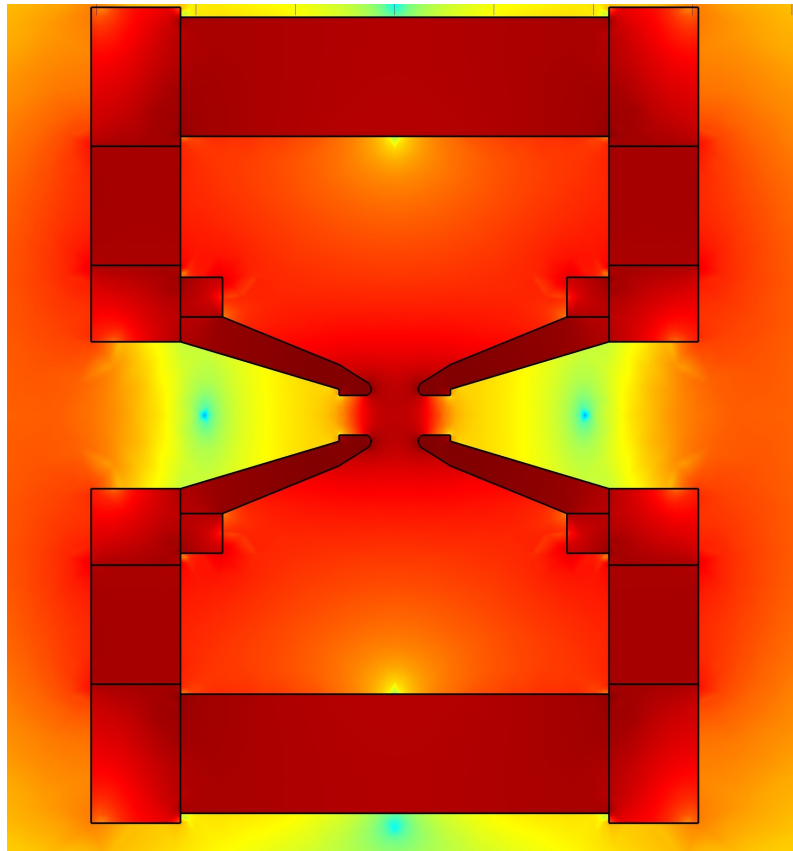
Figure 2.2: Simulation of the magnetic field magnitude using the software package COMSOL. The field strength is between $0\,\mathrm{T}$ (blue) and $0.7\,\mathrm{T}$ (dark red). From [10].
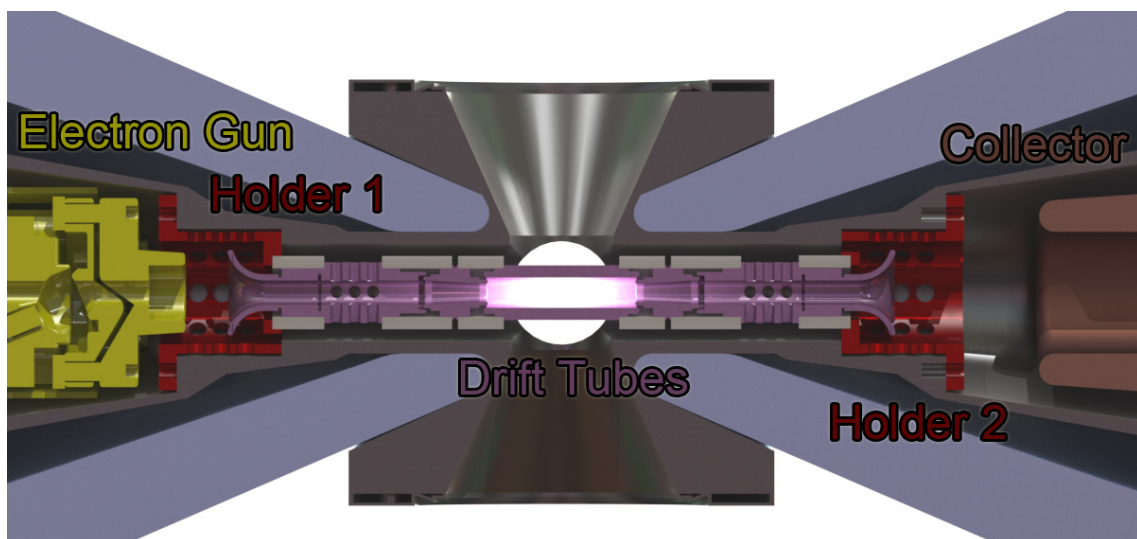

Figure 2.3: Overview of the ttEBIT's trapping region. The drift tubes (purple) are held in place by two holders (red). Ceramic rings isolate the different elements and hold them in place relative to each other.
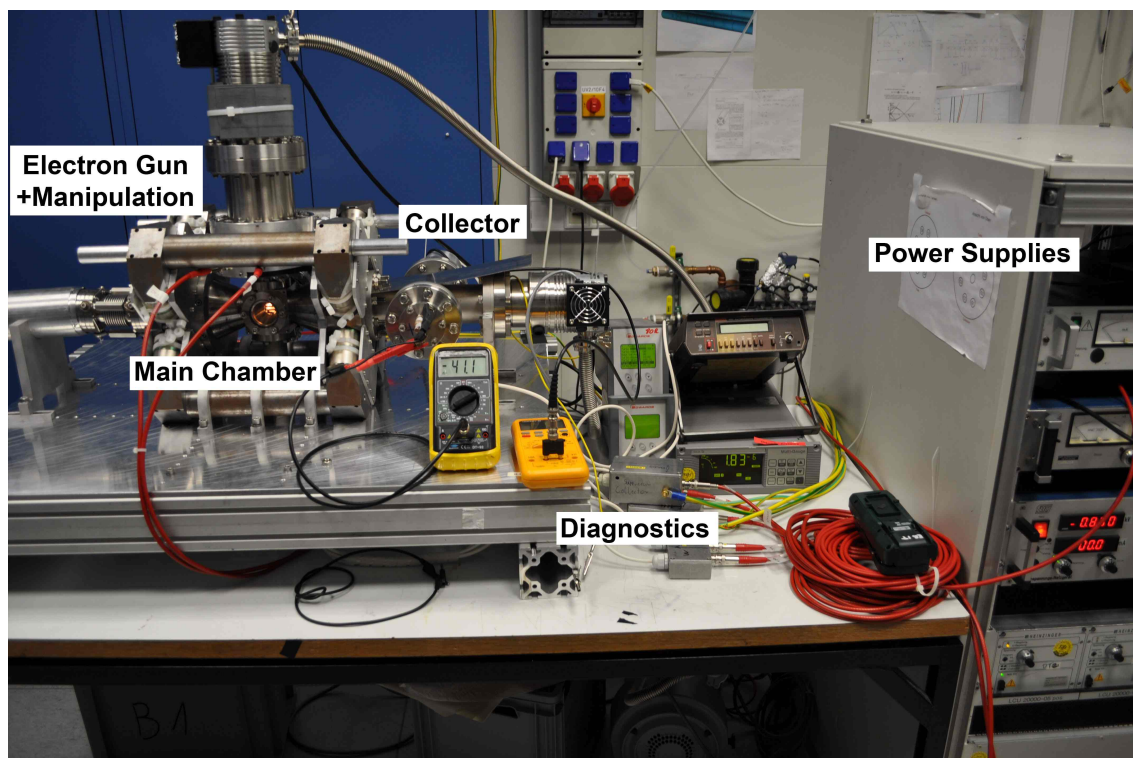
Figure 2.4: Photo of the *tt*EBIT. The electron gun can be manipulated using the bellows. All electrodes are connected to the power supply rack on the right.

where there is also a protective cover.

The radial positioning of the connectors allows for the connection of a turbomolecular pump on the same port. The port on the opposite side of the cube is used for the gas injection system which uses a needle valve, resulting in an effusive atom or molecular beam. This opposing arrangement of gas injection and turbo pump is desirable because the atomic beam will shoot straight into the pump, thus reducing the vacuum load in other regions of the *tt*EBIT. The third and fourth ports are used for optical access, for which a spectrometer can be used.

The collector is mounted on the opposite side of the electron gun, behind which a second turbomolecular pump is installed. This is important because there can be contaminants coming from the collector due to electron sputtering and it is crucial that as much as possible is kept out of the trapping region. The electrical feedthrough for the collector and extractor (see section 2.3) is also on this side of the *tt*EBIT.

The weights of the various components result in stresses and strains acting on the seals and weldings which can compromise the quality of the vacuum. Hence, supporting stands were designed and commissioned, which can take the weight of the different flanges connecting to the *tt*EBIT. These stands were mounted on an aluminium base plate, which was also designed to fix the *tt*EBIT in place. Furthermore, by mounting the plate on aluminium posts, access to the vacuum chamber from the bottom is possible (see fig. 2.4).
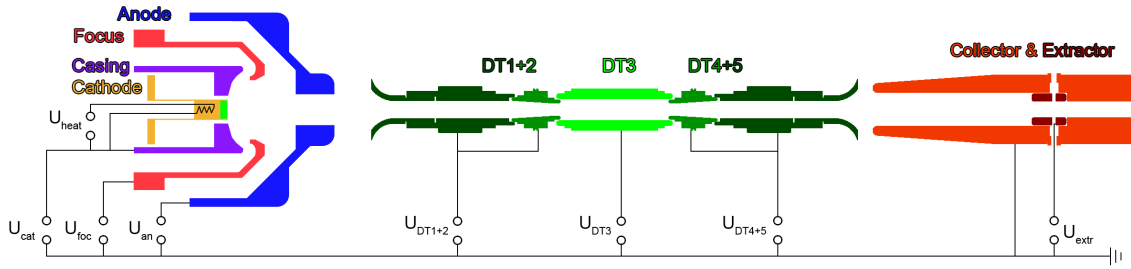
Figure 2.5: Circuit diagram of the *tt*EBIT. The cathode and its casing are put onto a potential U_{cat} and are heated with a heating current I_{heat}. The focus and the anode are put onto the potential U_{foc} and U_{an}, respectively. DT1 and DT2 as well as DT4 and DT5 share power supplies and the extractor is put on a potential U_{extr} while the collector is grounded. The electrodes are not to scale.
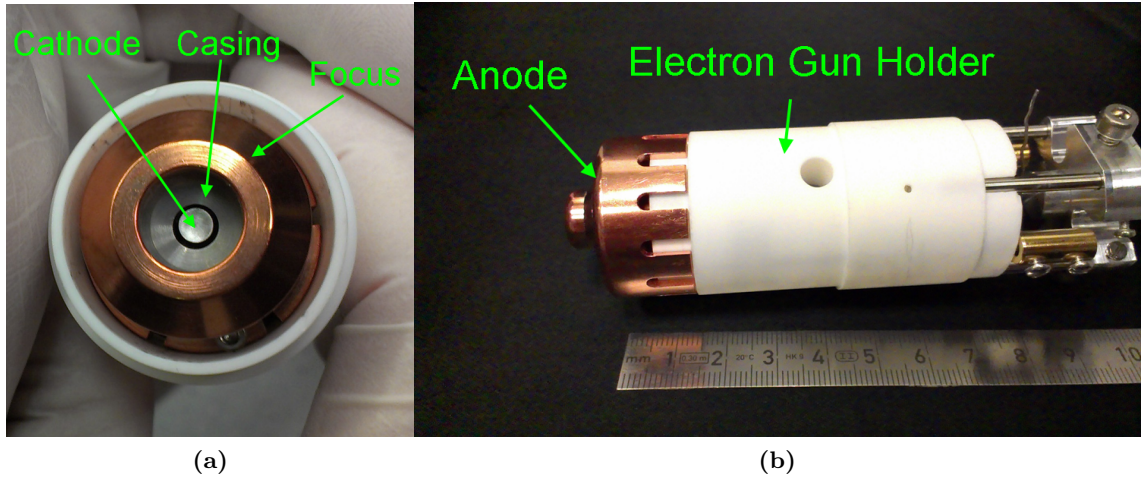

Figure 2.6: Photographs of the assembly of the on-axis electron gun used for first commissioning of the *tt*EBIT. In (a) the cathode, casing and focus electrode can be seen. The assembled gun is pictured in (b).

2.2 The On-Axis Electron Gun

For testing the present setup an on-axis electron gun (see fig. 2.6), that already exists in similar form in other Heidelberg EBITs (Hyper EBIT [9], Flash EBIT [8], HD-EBIT [22]), was used. For operation, four different power supplies are needed (see fig. 2.5). The cathode needs a $10\,\text{V}$, $3\,\text{A}$ power supply for the heating, which is put onto the bias potential of the cathode (U_{cat}), which can go down to a potential of $-3.5\,\text{kV}$. Any current being measured at this power supply (I_{cat}) is hence the total current of the electron beam. The power supply for the focus electrode has to be able to reach the same potential as the cathode in order to optimise the focusing of the beam. The anode is intended operate at voltages up to $3\,\text{kV}$, meaning that a maximum extraction voltage of $6.5\,\text{kV}$ could be reached. Unfortunately, the anode was apparently grounded due to a fault in the
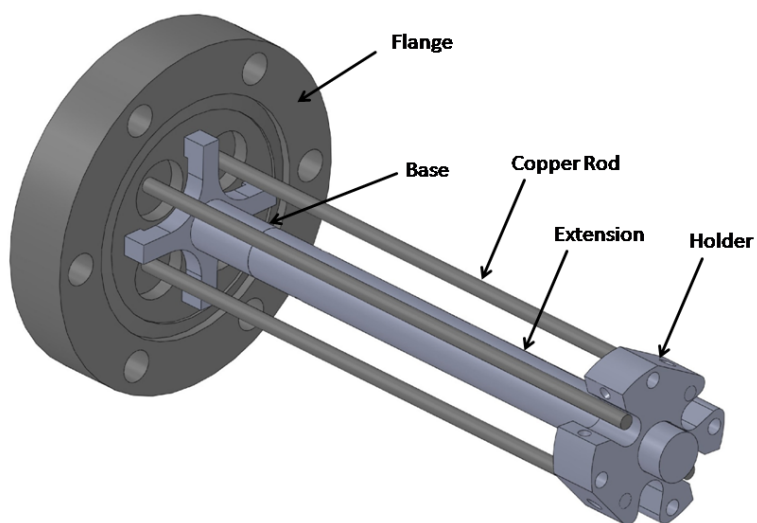
Figure 2.7: The mount for the on-axis electron gun. The long thin copper rods are the electrical feedthroughs, two connecting to the cathode and heater filament(current in and current out), one to the focus electrode and one to the anode. The gun is attached to the holder at the tip of the rod.
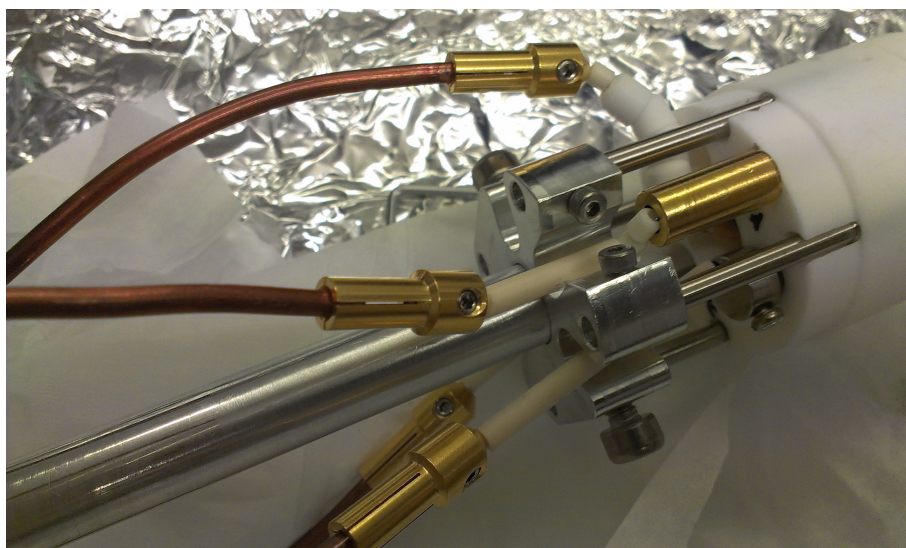

Figure 2.8: Photograph of the mount for the on-axis electron gun. The copper rods are connecting to the electrodes of the gun, which is held in place using screws.

(a) Assembled collector. The electron beam enters the collector from the right.

(b) Mounted collector seen from behind.

Figure 2.9: The collector with the extractor inside. The extractor is held in place by four screws, one which is also used to put the electrode on a potential. In (b) DT5 can be seen in the centre.

installation. This also means that there cannot be any current measurements being made.

The four outer drift tubes (DT1, 2, 4, 5) of the *tt*EBIT share two power supplies (one for each side), because DT1 and DT5 do not need an individual potential when using an on-axis gun (see section 4.2). The extractor is put on a potential U_{extr} while the collector is grounded through an amperemeter which measures the current of the electron beam hitting it.

A mounting system was designed and built for the on-axis gun which can be seen in fig. 2.7. It is based on a flange with 4 feedthroughs onto which a steel foot is welded. An extension is then screwed onto that foot, with a length that has to be chosen according to the vacuum components between the flange and the *tt*EBIT. For the present setup, a compact system was chosen with only a bellows and an adapter piece between flange and EBIT which is used for manipulation of the gun (see fig. 2.4). The adapter was designed to allow for as much leeway as possible for the manipulation of the gun. A holder is then screwed onto the extension, which holds the electron gun (see fig. 2.8).

2.3 The Collector

The collector (see fig. 2.9) is responsible for absorbing the electrons from the electron beam as well as to serve as a controlling electrode for ion extraction. Due to the energy deposition caused by the electron beam, the collector requires cooling. To improve thermal conductivity, copper was chosen as a material for the collector and the walls were chosen to be quite thick (5-10 mm). Thermal coupling was achieved by attaching the collector to two thick copper rods, which can be cooled from outside of the vacuum. These rods also serve two other purposes: the current from the electron beam flows to the ground through them and they are also used to hold the collector in place. Because of the collector weight it needed additional support to keep it concentric to the beam line axis (z-axis). It was therefore designed with three insulating polyether-ether-ketone (PEEK) inserts at the tip, which centre it inside the vacuum chamber.

An additional electrode (the extractor) is mounted inside the collector to keep electrons from going through it. The extractor is held in place by four screws that are insulated from the collector with ceramic spacers. By putting it on a potential lower than the cathode, it repels the electrons and forces them to hit the collector's inner wall. The extraction of
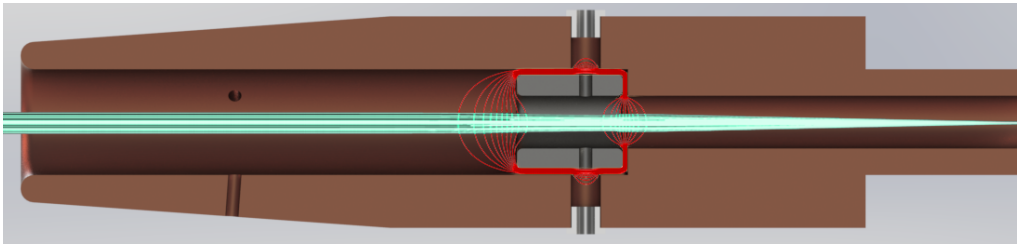
Figure 2.10: Cross section of the collector (brown) and extractor (grey) showing a SIMION simulation of ion extraction. The extractor is put onto a potential of $-100\,\mathrm{V}$ and the simulated particles correspond to Ir^{17+}, with a starting energy of $2.1\,\mathrm{keV}$, travelling from left to right (blue). This simulation does not include a magnetic field.

ions from the EBIT can be facilitated by using it as an electrostatic lens (see fig. 2.10).

The collector was designed to keep any impinging electrons as well as secondary electrons inside. The collector has a length of $190\,\mathrm{mm}$, in order to get as close to the drift tubes as possible.

Chapter 3

Characterisation of the Electron Beam

This chapter will discuss the key properties of the *tt*EBIT and describe the first commissioning of the apparatus using the on-axis electron gun. In this setup an old cathode is used for testing the functionality of an electron gun in the new EBIT.

3.1   Simulations

To predict the functionality of the design, TriComp was used to simulate the electron beam under cylindrical symmetry. To get reasonable data from electron path simulations it is crucial to know $\boldsymbol{E}$ and $\boldsymbol{B}$. While $\boldsymbol{E}$ can be readily simulated with TriComp, calculating $\boldsymbol{B}$ poses more of a challenge because it is important that it is as close to the real magnetic field inside the *tt*EBIT as possible. Simulations using the software package COMSOL (from [10]) and TriComp agree well for $\boldsymbol{B}$ close to the trap centre, but there are considerable deviations from the measured $\boldsymbol{B}$ around the electron guns position (see fig. 3.1). For a better fit to the real $\boldsymbol{B}$, the TriComp simulation was adjusted by adding several coils to the simulation and setting their current such that the point of lowest $\boldsymbol{B}$ fits well with the measured data. Adjusting the field like this has the downside of unrealistic $\boldsymbol{B}$ next to the added coils (A and B in fig. 3.1), but given the magnitude of these deviations relative to their surroundings, it is estimated that their effect is negligible. This is supported by their distance to the relevant regions: the cathode and the trap centre.

A typical simulation can be seen in fig. 3.2: The gun sits on the left, shooting into the drift tubes, with the simulation ending at the trap centre. For evaluating this simulation, two factors have to be taken into account: The perveance of the electron gun as well as the beam diameter at the trap centre.

The simulations show that for the present electron gun the perveance is strongly dependent on the focus electrode potential because it is in front of the cathode (see fig. 2.6a), which means that it is able to contribute to the electron emission when put onto a positive bias with respect to the cathode. TriComp simulations predict that this voltage is limited because it affects the convergence of the beam. For example, for an extraction voltage of $5.5\,\mathrm{kV}$, a greater potential difference between cathode and focus than $300\,\mathrm{V}$ would strongly degrade the quality of the beam. This corresponds to a predicted extraction current of
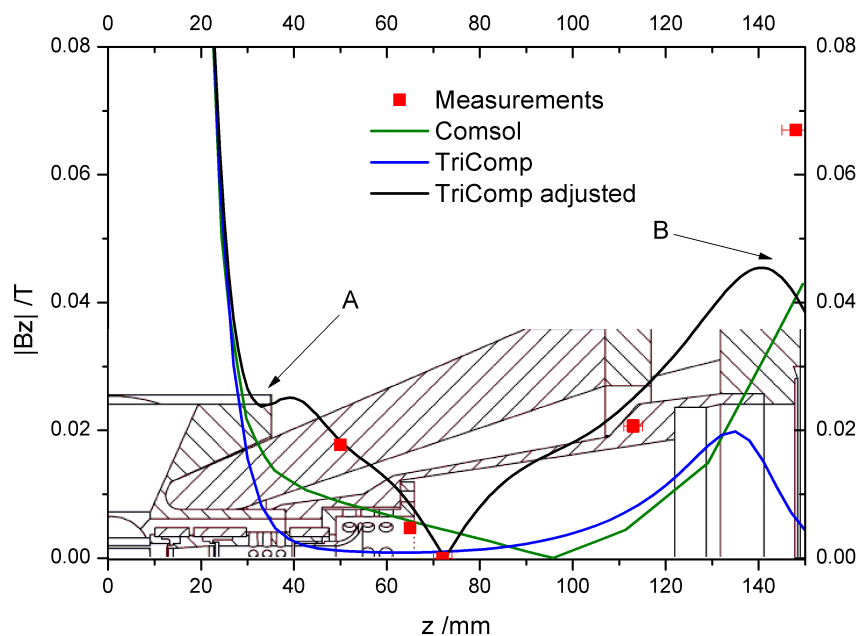
Figure 3.1: Different simulations of the magnetic field inside the *tt*EBIT. The 'TriComp' (blue) and 'Comsol' (yellow) data was calculated using the geometry of the magnetic setup, while the 'TriComp adjusted' data was designed to fit to the measured data points. Error bars on the measurements are to small to be shown.
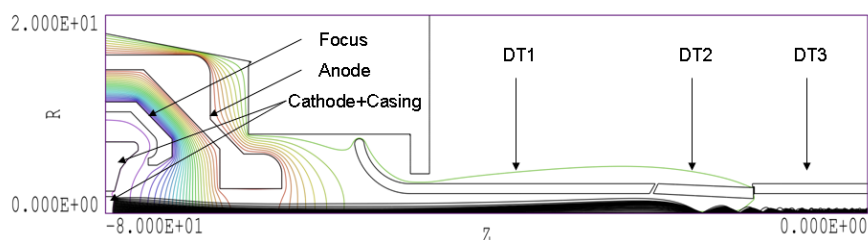

Figure 3.2: TriComp simulation of an on-axis electron beam from the cathode to the trap centre. The potentials of the cathode, focus and anode are $-3.5\,\text{kV}$, $-3.2\,\text{kV}$ and $2\,\text{kV}$ respectively. DT1 and DT2 are at $0.2\,\text{kV}$ and the space charge limited extraction current is $29\,\text{mA}$. The units are in mm.
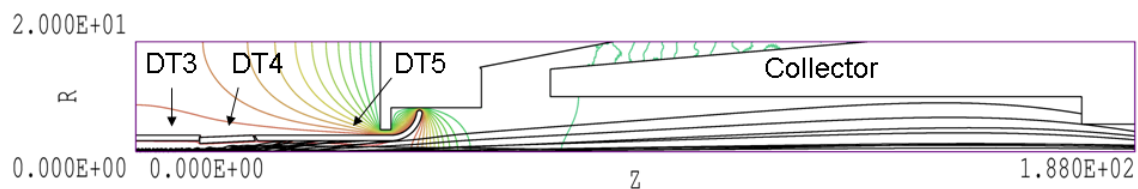
Figure 3.3: TriComp simulation of an on-axis electron beam from the trap centre to the collector. The space charge limited extraction current is $29\,\text{mA}$ and the extractor electrode is not included in the simulation. The units are in mm.

29 mA, or a perveance of 0.071 µperv.

Another important feature in fig. 3.2 is the expansion of the beam in DT1-2 due to the space charge effect. This leads to the "bumps" in DT2-3, which show that the maximum compression of the beam is not being reached. This problem arises because of the long path length between the electron gun and the significant increase in B. Overcoming this is very important if the *tt*EBITs full potential is to be reached. One solution could be to adjust the magnetic system in such a way that stretches B closer to the electron gun. A simpler way is the use of an electrostatic lens, which is discussed in ch. 4.2.

Behind the trap centre a strong divergence of the electron beam is predicted (see fig. 3.3). Because of the length of drift tubes a large fraction of the electrons impinge on DT 5. Furthermore even though B is very weak beyond the holder, it is strong enough to compress the beam inside the collector, such that the electrons go through it. This behaviour would be a severe problem because a high energy electron beam can damage instruments. Furthermore the energy deposited in DT 5 would mean that its temperature builds up over time because it has bad thermal conductivity to the outside, eventually resulting in damage.

3.2 Electron Beam Behaviour

3.2.1 The Cathode

A critical part for the successful creation of an electron beam is the cathode, because it defines the maximum current that can be reached. Barium-impregnated cathodes for high current electron beams are usually quite fragile and need to be handled with care: when in contact with air they absorb moisture and their surface gets contaminated. Furthermore, the pressure at an activated cathode (P_{cat}) is not supposed to exceed 1×10^{-6} mbar [23]. Since the utilized test cathode was in contact with air for a long period of time (over one year), it was expected that its electron output would be severely diminished.

When heating up the cathode, one has to be careful because a too short heating voltage (U_{heat}) ramp up time can poison the cathode beyond repair. This is because the moisture inside the cathode would not be able to leave quickly enough and it would form hydroxides and carbonates which reduce emission capabilities and cause blistering and cracking of the tungsten emitter surface [23]. While the outgasing process is usually supposed to be done within a few days [23], the ramp up time turned out to be 16 days for the cathode which was used for testing. This long time arises from the limitation on P_{cat}, because it increases with an increase in U_{heat} since higher temperatures mean more outgasing and the pumping speed is limited.

A typical pressure spike can be seen in fig. 3.4. Here, the measured pressure (P) is continually falling until U_{heat} was increased from 2.4 V to 2.6 V, which resulted in a drastic pressure increase after which P slowly falls again. Fig. 3.4 also shows the noise of the measurements, which represents the maximum and minimum values that were measured in the time interval the average value was calculated over (about one second). This ensures that no short P spikes were missed when taking the measurement. It is worth noting that even for a severely contaminated cathode the measured pressure increase due to outgasing seems to be too much. It is therefore expected that at higher temperatures the majority of the increase in P came from the moisture inside the insulating casing of the electron
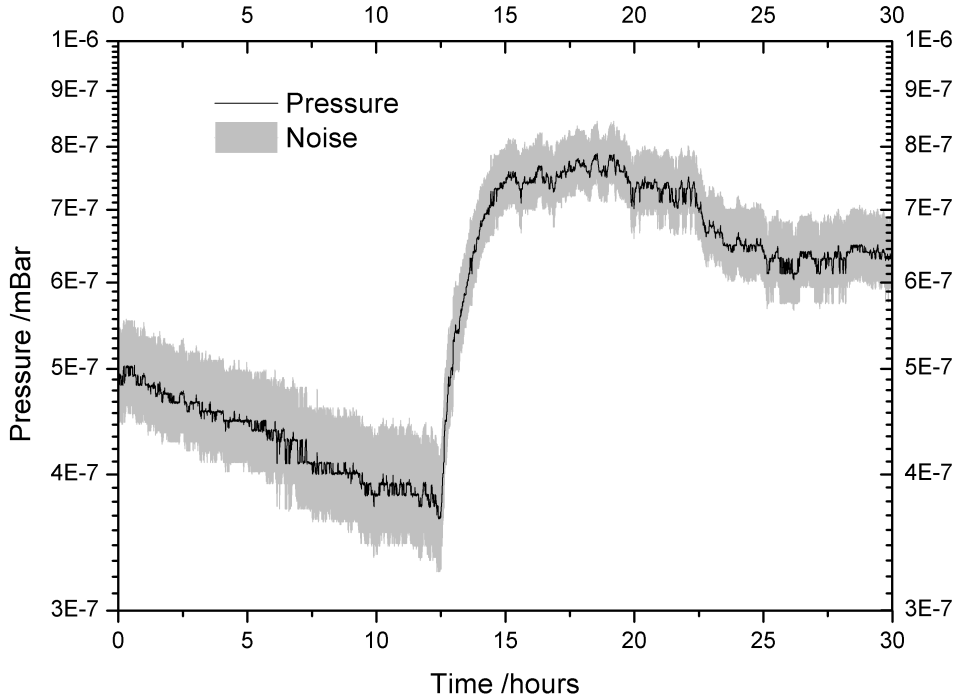
Figure 3.4: Typical graph showing the pressure increase when heating up the cathode on the 21.05.2013. The heating voltage was increased from 2.4 V and 0.95 A to 2.6 V and 0.98 A at $t \approx 12.5$ h. The grey area shows the range of measured values over which each data point was averaged.

gun. This casing was also stored in air and is made of MACOR, which can hold moisture much better then any metal. Note that P is not necessarily the same as P_{cat} because the pressure gauge is mounted at a different position as the cathode.

The cathode was found to operate stably at $U_{heat} = 8.5$ V with $I_{heat} = 1.45$ A. While initial emission currents (I_{cat}) were in the µA range, this improved considerably over time leading to a measured I_{cat} of 2.2 mA about one week after reaching operational temperature. This can be attributed to ions being created from electrons hitting residual gas, which are then accelerated towards the cathode, sputtering its surface and removing impurities. I_{cat} can be measured at the power supply for the cathode potential. This yields the total extracted current, but gives no information about its trajectory. For more insight about the behaviour of the electron beam, the current at each electrode has to be measured individually, ideally showing that the entire emitted current hits the collector. It was found that by installing a magnetic plate over the collector, the measured collector current (I_{coll}) roughly doubles. This can be explained with TriComp's prediction about the electrons being focused inside the collector: The plate disturbs the symmetry of B inside the collector preventing the electrons from going through.
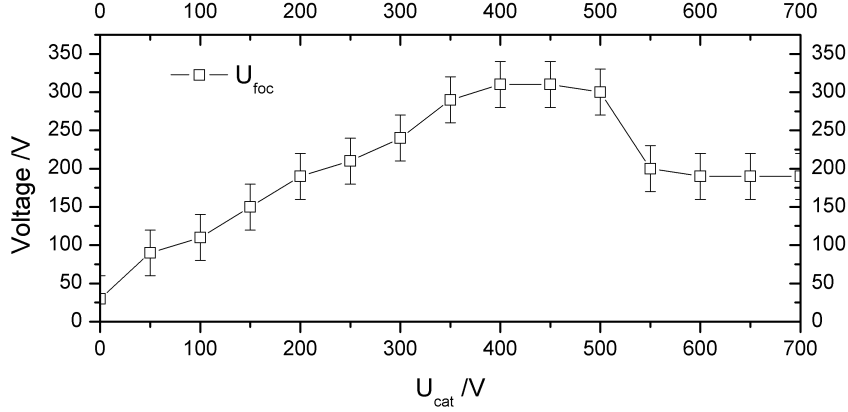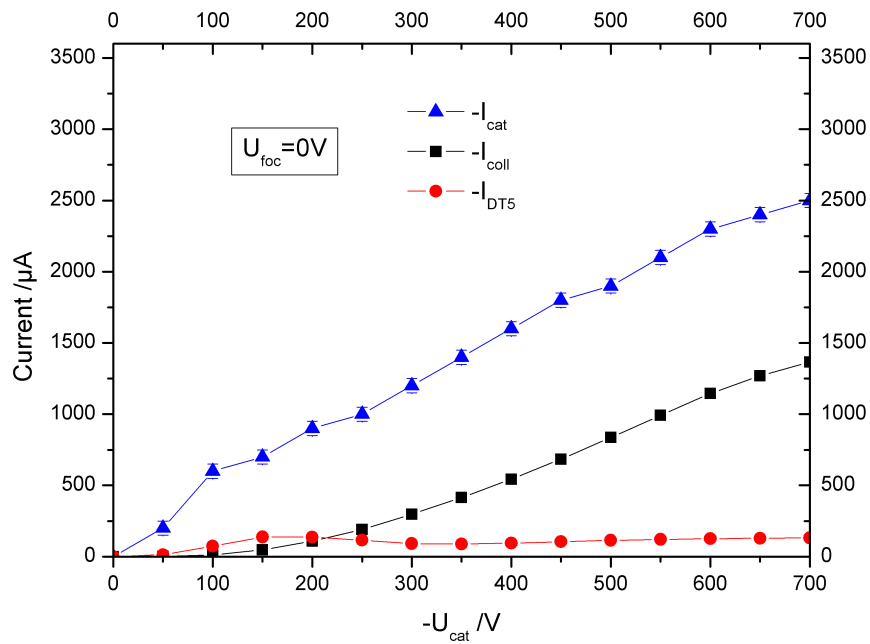
Figure 3.5: Measurements of the focus electrode potential (U_{foc}) as a function of the cathode potential (U_{foc}). The focus electrode power supply was turned on, with a set potential of $0\,\text{V}$. There seems to be an off-set of about $25\,\text{V}$ between the reading and the actual voltage, as can be deduced from the first data point.

3.2.2 Current Measurements

Further measurements showed that there is a negligible amount of electrons hitting DT1-4, while the measured current at DT5 (I_{DT5}) can under certain conditions even exceed I_{coll}, which agrees well with the simulations. For initial characterisation, all the electrodes were grounded: collector and DT5 directly through a multimeter, and the other electrodes through their power supplies, or directly to ground. I_{cat} increases with increasing U_{cat}, i.e. with increasing extraction voltage. This behaviour is predicted for space charge limited extraction with $I_{cat} \propto U_{cat}^{1.5}$ (see sec.1.2). This is inconsistent however, with an observed strong dependence of the emission current on U_{heat}, because space charge limited emission is independent of the cathode temperature. This can be explained when assuming the cathode emission is source limited, suggesting that $I_{cat} \propto e^{\sqrt{aU_{cat}}}$ with a being a constant (see sec. 1.2). Hence, there is no meaning in talking about the perveance of the gun, because it is only defined for a space charge limited emitter.

It was found that the power supply for the focus electrode charges itself up when the electron beam is turned on, which can be observed in an increasing measurement of the focus potential (U_{foc}) despite setting the focus electrode power supply to $0\,\text{V}$. Interestingly, U_{foc} does not continually increase with increasing U_{cat} (and hence increasing I_{cat}), but rather peaks at around $U_{cat} = 450\,\text{V}$ after which it falls to a seemingly constant value (see fig. 3.5). An increase in U_{foc} is predicted to improve the focusing of the beam, which would mean that less electrons hit the focus electrode, but this cannot explain an observed sudden drop in U_{foc}. This behaviour is due to the charging up of the electrode by stray components of the beam and depends on the inner resistance of the power supply. For better reference, other measurements were done with U_{foc} being set at a higher potential, because it would then be independent of U_{cat} as well as with the focus electrode being directly grounded for comparison.
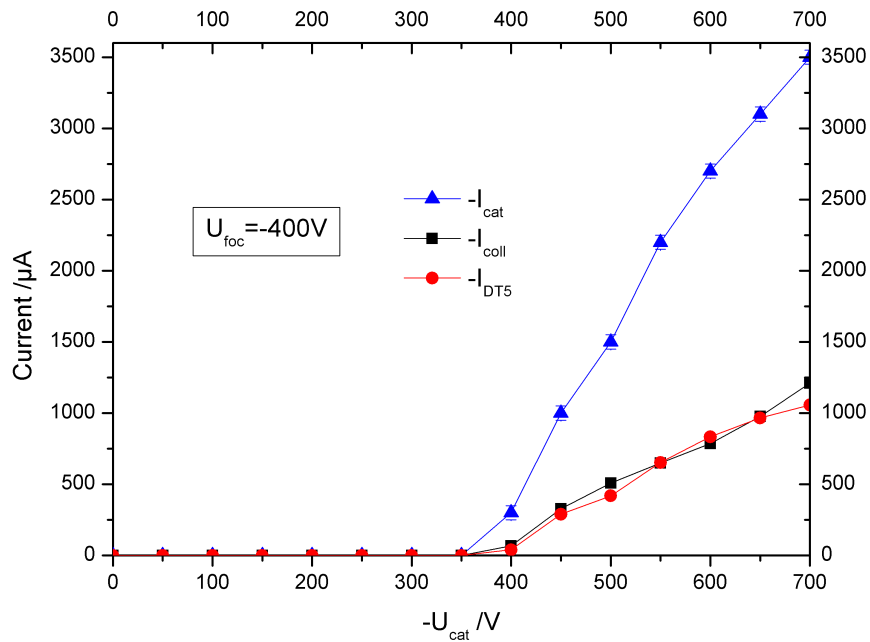
(a) Grounded focus electrode

(b) $U_{foc} = -400\,\mathrm{V}$

Figure 3.6: Dependence of the extraction current on the extraction voltage. Currents were measured at the cathode (I_{cat}), the collector (I_{coll}), and DT5 (I_{DT5}). Measurements were done at $U_{foc} = 0\,\mathrm{V}$ (top) and $U_{foc} = -400\,\mathrm{V}$ (bottom). Error bars are partly smaller than the symbols.

Collector

When directly grounding the focus electrode, I_{DT5} and I_{coll} behave similarly at low energies ($U_{foc} < 150\,\text{V}$), but start to diverge strongly for higher energies: while I_{DT5} stays at a constant value of about $100\,\mu\text{A}$, I_{coll} continues to rise proportionally with I_{cat} (see fig. 3.6a). The relation between I_{coll} and I_{cat} is straightforward, since a constant fraction of the emitted beam hits the collector. This also means that a significant fraction of the beam is lost somewhere along the way. Some part of the beam hits the focus electrode, but it is not enough to explain the significant difference between I_{coll} and I_{cat}. It is therefore presumed that the rest of the electrons hit the anode, where the current cannot be measured due to a fault in the installation. This could become a problem since an intense energy beam could cause damage to the anode, but it still needs to be confirmed.

Putting the focus electrode on a negative potential and thereby decreasing the extraction voltage has several effects on the electron beam. The extraction can only start once $U_{cat} < U_{foc}$, after which the extracted currents increases more rapidly than for a grounded electrode (see fig. 3.6b). This behaviour was unexpected since a lower extraction voltage usually means less extracted current. A possible explanation could be the larger voltage between the cathode and the other electrodes at the same extraction voltage. For example, if the focus is grounded, the extraction voltage at $U_{cat} = -300\,\text{V}$ is $300\,\text{V}$ and the voltage between the cathode and the collector is also $300\,\text{V}$. If $U_{foc} = -400\,\text{V}$, the extraction voltage is $300\,\text{V}$ when $U_{cat} = -700\,\text{V}$, resulting in a voltage between cathode and collector of $700\,\text{V}$. This strong dependence of the extraction current on the potential of other faraway electrodes was already observed in other EBITs and can also be seen in the ttEBIT under different circumstances: By changing only the extractor electrode potential, I_{cat} also goes down despite the cathode's local electric field being unaffected.

In addition to this, the cathode emission is also dependent on the emission surfaces integrity: the current extraction is based on the Ba atoms at the cathode surface. These can get sputtered off due to positively charged ions that are attracted to the cathode. This effect gets stronger with a stronger extraction voltage, so if for example $U_{cat} = -700\,\text{V}$, the emission is stronger with $U_{foc} = -400\,\text{V}$ than with $U_{foc} = 0\,\text{V}$, but combined with the aforementioned effect, $U_{cat} = -300\,\text{V}$ and $U_{foc} = 0\,\text{V}$ leads to a smaller current than in either of those cases.

DT5

Another important difference between fig. 3.6a and fig. 3.6b is the behaviour of I_{DT5} as it drops to a constant value when $U_{foc} = 0\,\text{V}$, but rises like I_{coll} when $U_{foc} = -400\,\text{V}$. Some insight about the relevant processes can be gained when looking at the current's time dependence when switching the extraction on. When the focus electrode is grounded, I_{DT5} rises within a second to a peak, but drops just as quickly, whereas I_{coll} continues to rise for a few more seconds after which a slight decrease can be observed(see fig. 3.7a). When $U_{foc} = -400\,\text{V}$ however, I_{DT5} stays nearly constant while I_{coll} starts to decrease immediately, if only by a slight amount (see fig. 3.7b).

The timescale on which these changes take place, suggests that the charging up of some component plays a role, which influences the focusing of the beam. This would agree with the initial rise in I_{coll} in fig. 3.7a, since a better focusing would mean less electrons hit DT5 and more hit the collector, but then the rise would be expected to be more substantial.

So a more thorough investigation of the electron trajectories is necessary, which can be done by making sure that no electrons hit anything that is directly grounded. This would entail fixing the electron gun so that the anode is no longer grounded and installing a metal plate at the back of the collector so that no electrons could possibly go through. The drop in I_{coll} after one minute of turning the electron beam on can be explained with the gradual sputtering of the Ba, which will eventually lead to a constant current, because of the diffusion of Ba from the Ba reservoir inside cathode.

These approaches were not attempted, since the unexpectedly long conditioning time for the cathode would have compromised the other systematic tests of the apparatus.
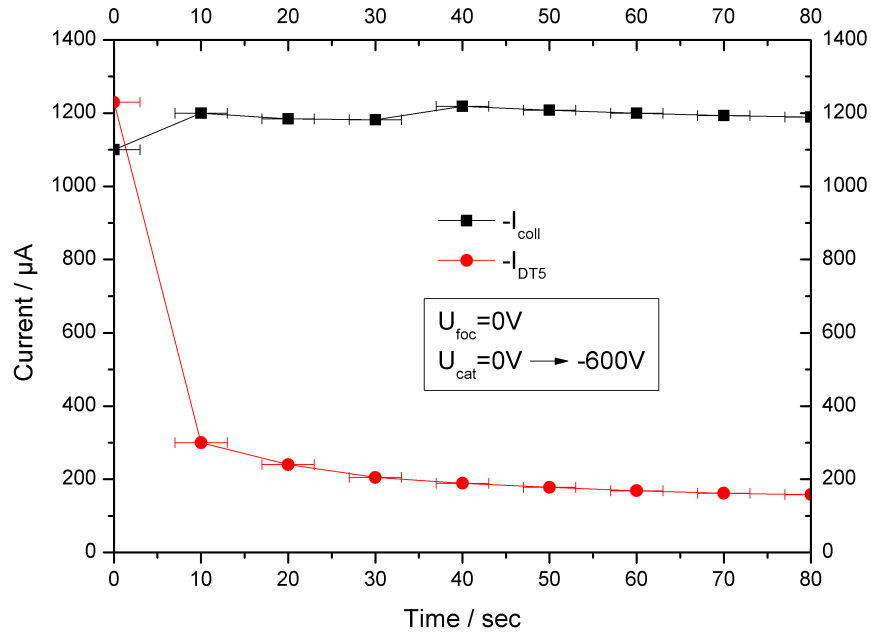
(a) Grounded focus electrode
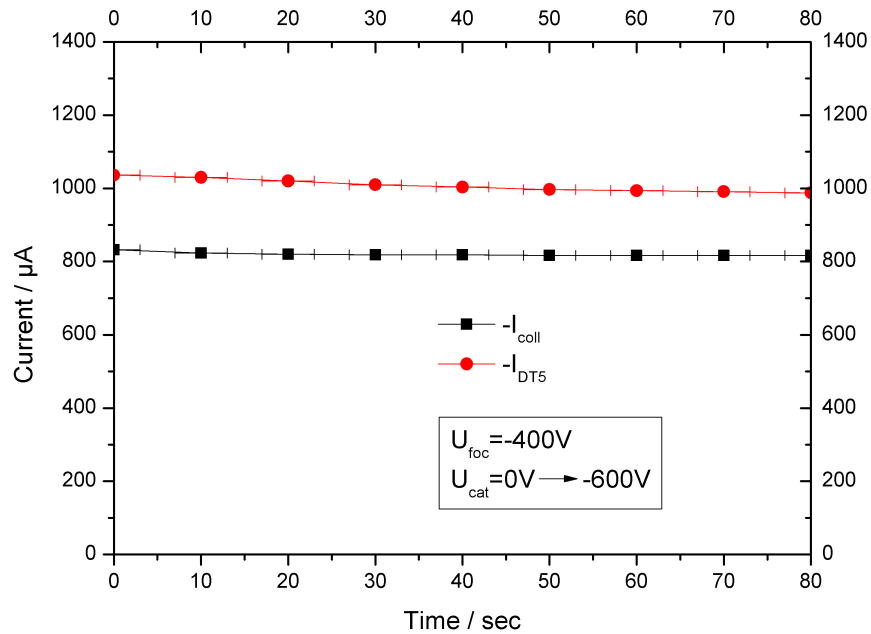
(b) $U_{foc} = -400\,\text{V}$

Figure 3.7: Time dependence of measured current at the collector (I_{coll}) and DT5 (I_{DT5}), after switching the cathode potential from $0\,\text{V}$ to $-600\,\text{V}$ at $t = -1\,\text{s}$.

Chapter 4

The Off-Axis Electron Gun

The method of resonant laser spectroscopy is currently the most precise spectroscopic technique in physics [8], and meanwhile there are reports of first the measurements of electronic transitions under laser excitation in EBITs (e.g. [7], [8], [24], [25]). In those pioneering experiments, photoexcitation was achieved by introducing a laser from the collectors side of the EBIT to maximise the overlap with the electron beam. Because the laser could damage the cathode, the electron gun is then mounted slightly shifted from the main axis, so that the laser hits an specially constructed shield [24]. Another solution would be the use of an off-axis electron gun (OAG), an electron gun with the feature of leaving the z axis free of any obstructions. This could be achieved by positioning the cathode next to the z axis and then steering the electron beam onto the right path (see fig. 4.2a). This approach has the additional advantage that the photon beam can be used at a second experiment behind the *tt*EBIT.

This is the first time that an OAG is intended for the use in an EBIT, so the gun had to be developed from scratch. The OAG was designed for the geometry of the *tt*EBIT, but it can be used in other EBITs as well. This chapter covers the electron beam manipulation first (sec. 4.2) and then describes the layout of the OAG (sec. 4.3).

4.1   Overview

The electrodes inside the OAG are largely based on electron beam simulations made with SIMION 8.0. As opposed to a normal electron gun, the electron beam of an OAG needs to be steered into the z direction because the electrons are extracted at an angle to the z axis. Additionally, the beam has to be collinear to the z axis to ensure that a laser used for photoionisation overlaps with it. Other important factors for the design of the electrodes were the perveance of the gun as well as good control over the focussing of the beam.

First designs of the OAG were based on steering the electron beam using the focus electrode as inspired by [26]; an example of which can be seen if fig. 4.1a&b. It was thought that by splitting the focus electrode into two parts – a bottom and a top part – the angle of the beam could be controlled by putting the top part on a negative bias, such that it would hit the centre of the anode. However, it can be seen that the path length between cathode and anode is too short for the beam to reach the z axis, resulting in the beam hitting the anode. So, bending the beam onto the right track should not be done by
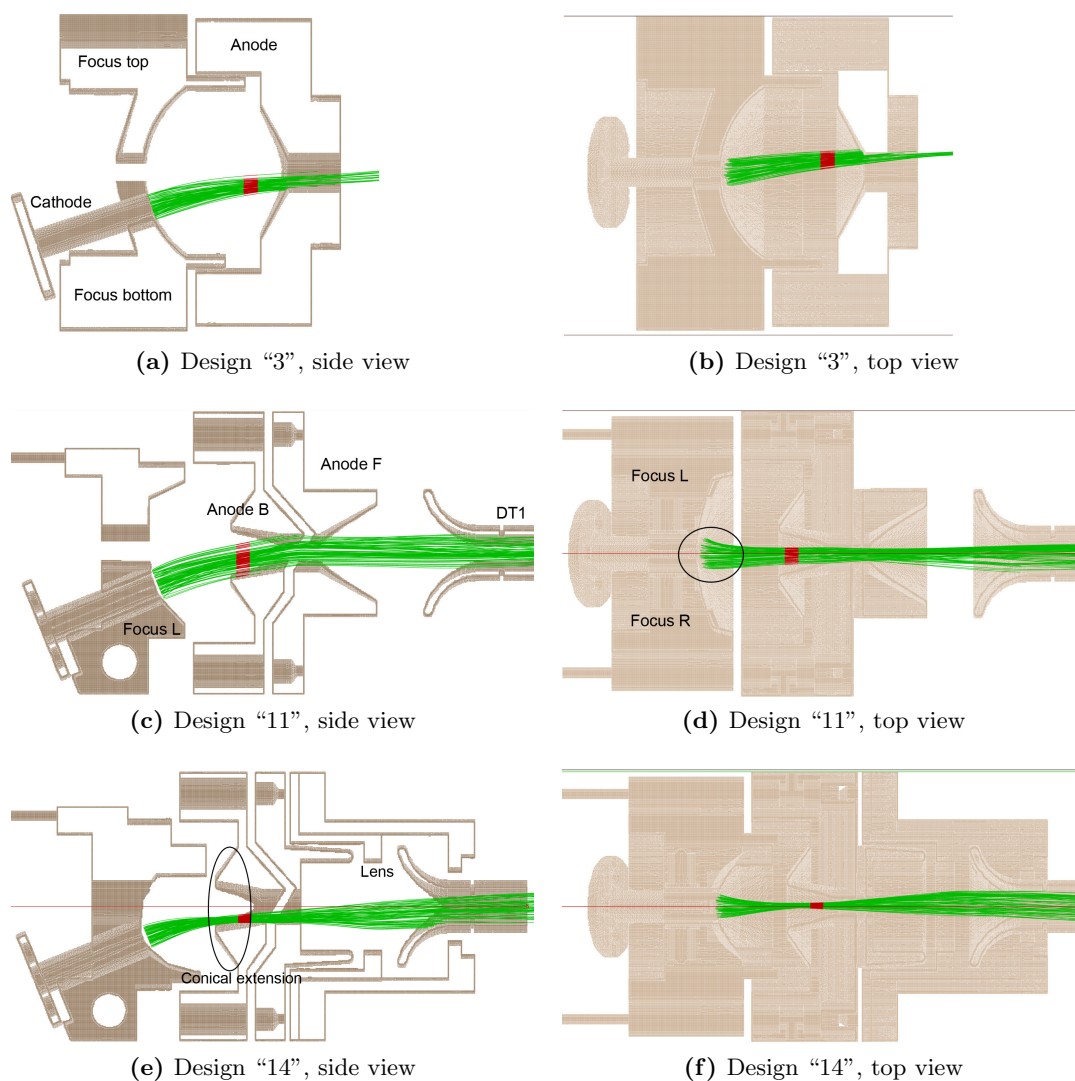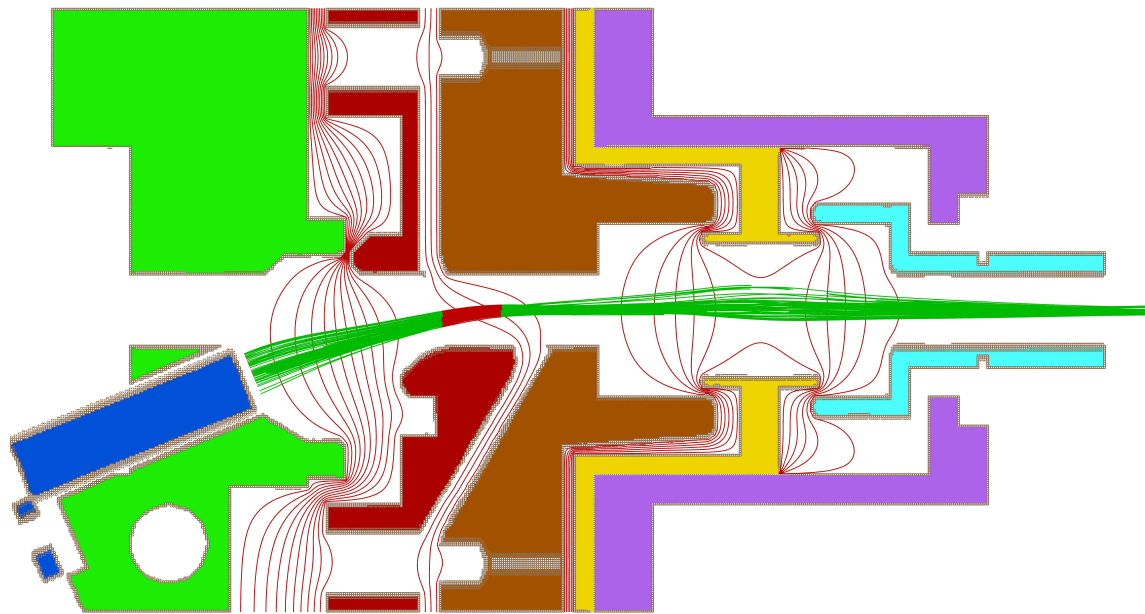
(a) Design "3", side view

(b) Design "3", top view

(c) Design "11", side view

(d) Design "11", top view

(e) Design "14", side view

(f) Design "14", top view

Figure 4.1: SIMION simulations of three different OAG designs, each from a side view (a, c, e), and top view (b, d, f). The green lines are electron trajectories, with the red area indicating a region with $|B| \leq 0.9$ mT. For the side views only the central slab of geometry is shown, while the top views show the bottom half of the OAG. Designs are labeled 1 through 19, three of which are shown here.

(a) Final design, side view
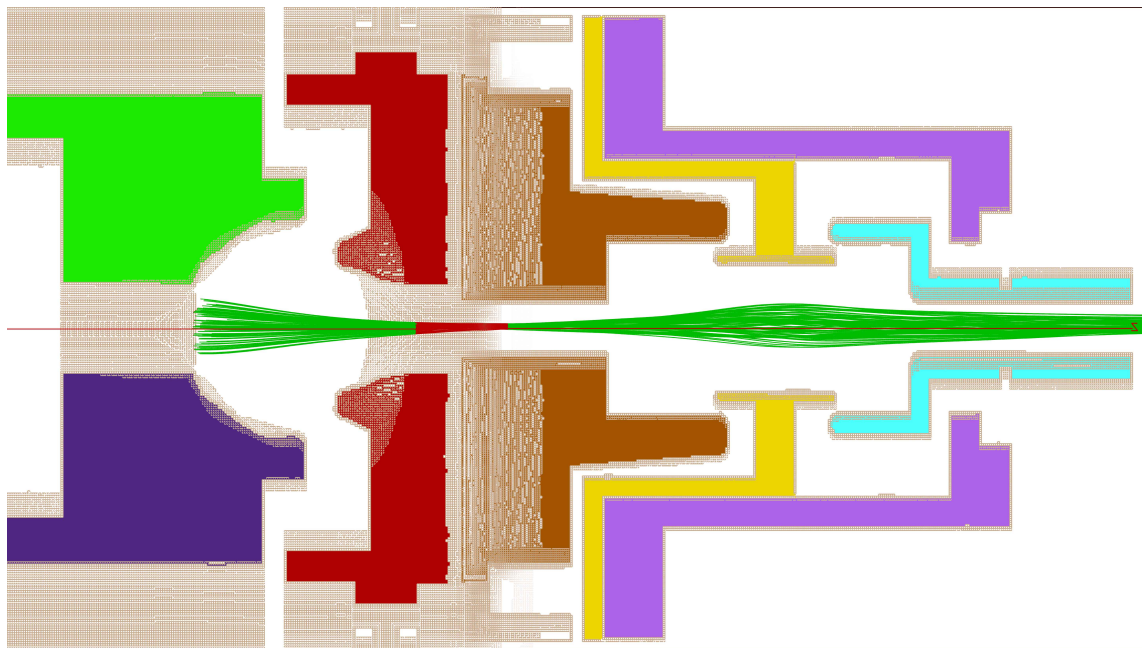
(b) Final design, top view

Figure 4.2: Electron beam simulation using SIMION. The potentials are as follows: cathode (blue)=−3.6 kV, focus L (green)=−3.45 kV, focus R (lilac)=−3.55 kV, anode B (red)=2 kV, anode F (brown)=0.25 kV, lens (yellow)=−2.8 kV, holder (purple)=0 kV, DT1 (blue)=0.1 kV. The green lines are electron trajectories, with the red area indicating a region with $|B| \leq 0.9$ mT.

the focus electrode, but rather by the anode. This can be achieved by splitting the anode in two with a diagonal cut, yielding one electrode on the back (anode B) and one on the front (anode F) (see fig. 4.1c).

The first simulation also highlights a different problem, which can be seen in fig. 4.1b. The electrons have a velocity component in the xy plane while flying from the cathode to the anode. Now, because $\boldsymbol{B}$ points in the z direction ($\boldsymbol{B} = B_z \equiv B$) there is a Lorentz force acting on the electron beam that pushes it to the side. This was counteracted by splitting the focus electrode into two parts: focus L and focus R. This solution has only limited use though, because the achievable sideways force is strongest at the emission surface of the cathode and drops rapidly with increasing distance (circle in fig. 4.1d). It is thus very important to reduce magnetic field inside the gun as much as possible. It was approximated that the magnetic shielding of the gun reduces B by 50 %, which is a conservative estimate given the data from the magnetic shielding supplier 'Less EMF Inc.' [27]. Using the reduced B in the region of the OAG, in the simulations show a good mitigation of the sideways velocity component without disturbing the roundness of the beam (see fig. 4.2b and fig. 4.1f).

4.2   Electron Extraction

In order to optimise the perveance of the OAG it is important to have the anode as close to the cathode as possible. The anode aperture has a minimum size defined by the diameter of the an on-axis laser. To meet this requirement, the aperture was chosen to have a diameter of 4 mm. This also restrains the height of the tip of the cathode, because it has to be at least 2 mm below the z axis, so it does not obstruct the laser. Now, for this design, it is intended to use a commercial cathode from HeatWave Labs Inc. [13] with a diameter of 3.4 mm (model 101157 [28]), which means that the cathode diameter is about the same size as the anode aperture. Given the cathode diameter, simulations showed that mounting the cathode at an angle of 22° (defining the extraction axis) yields good extraction results. A lower angle would mean that the anode had to be further back in order for the beam to reach the z axis, or otherwise it would hit the anode. A steeper angle means divergent behaviour of the beam at the tip of the gun.

With the extraction axis defined, it can be seen that the ideal position of the anode can also be determined (see fig. 4.3). Further improvement of the perveance can be achieved using a conical extension at the anode (see fig. 4.1e), which is also often used in on-axis high flux electron gun designs [14]. It has a larger aperture at the tip, so that it can be closer to the cathode without blocking the way for the incoming electrons. However, as can be seen in fig. 4.1e, the pull into the z direction starts too early, so the beam does not reach the centre of the aperture. This problem can be solved by having this extension (or ledge) cylindrically symmetric about the extraction axis ('Ledge A' in fig. 4.3).

As previously mentioned, the bending of the beam is controlled by putting a voltage between anode B and anode F. This is ideally done by placing the diagonal cut such that the electron beam is directed to the z direction by putting anode F on a negative bias compared to anode B (e.g. from top left to bottom right in fig. 4.2a). This way, anode B can be put on as high a potential as possible without the problem of having to apply an even higher potential to anode F. Placing the cut this way has the additional advantage of
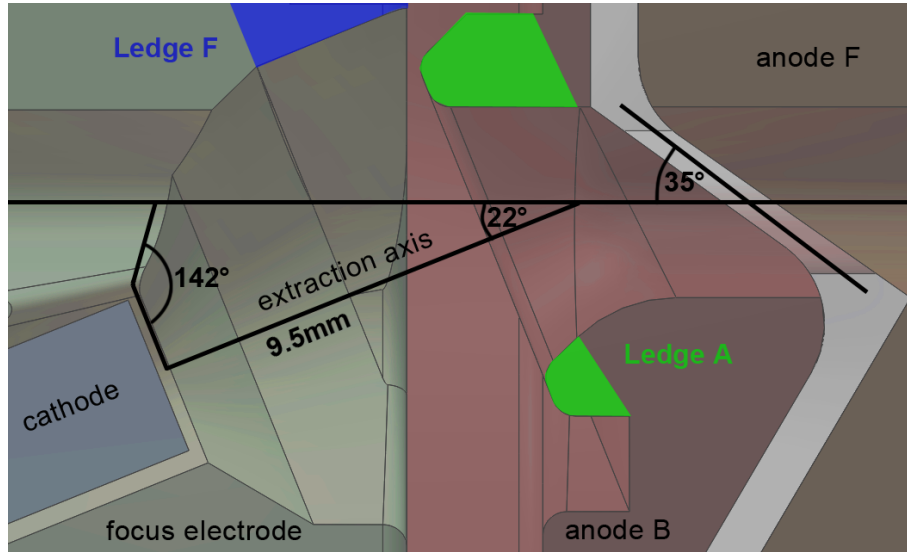
Figure 4.3: Side view of the OAG showing the relevant dimensions of the design. The angle and size of the cathode (grey) define the extraction axis, which cuts the z axis near the beginning of anode B (light red). The focus electrode is light green and anode F is light brown.

reducing the path difference between the different trajectories of the beam, which might lead to imbalanced space charge.

To reduce the number of electrons hitting the anode, the focus electrode was also chosen to be cylindrically symmetric about the extraction axis (see fig. 4.1c&e and fig. 4.3). For further improvement, the shape of the focus electrode was chosen such that the beam focuses at its bending point between anode B and anode F (compare fig. 4.1c to e). The focus also has a ledge similar to the anode, but this one is asymmetric ('Ledge F' in fig. 4.3), which serves the purpose of giving the trajectories a slight curvature, reducing the entrance angle at anode B (see fig. 4.2a).

The perveance of the gun can be estimated using TriComp by approximating the gun to be cylindrically symmetric about the extraction axis (see fig. 4.4). This results in a predicted perveance of 0.2 µperv, which can be compared to the perveance of the HD-EBIT electron gun, which is 1 µperv [22]. The OAG lower value mainly stems from the larger distance between cathode and anode which comes from the angular inclusion of the electron beam. The distance between the two electrodes can be reduced by using a cathode with a smaller diameter, making the aberrations would be less severe. It remains to be shown whether this would overcome the downside of having a smaller extraction area.

Since the electron extraction puts many geometrical limitations on the different electrodes, it is useful to include a lens behind the OAG. Normally the focus electrode can be used to control the focussing of the beam, but it already has a fixed focus point inside the gun itself, at the bending region of the beam. For this reason the anode F has a tip that lends itself to electrostatic lensing. Since it is important to have the gun as close to the trap centre as possible (see sec. 4.3) this additional lens is intended to be put inside the holder (purple in fig. 4.2), making (a redesigned) DT1 part of the lens (light blue in fig. 4.2). This approach has the additional advantage of easy installation, because two
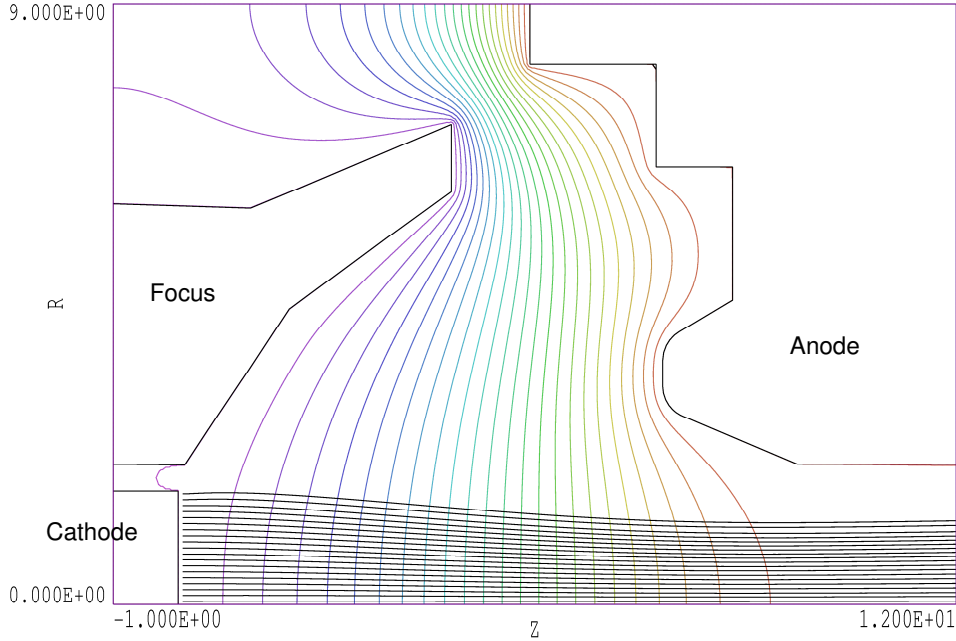
Figure 4.4: TriComp simulation of the extraction axis using cylindrical symmetry. The extraction voltage is $4.5\,\mathrm{kV}$ resulting in a current of $59\,\mathrm{mA}$. The units are in mm.

of the three necessary parts are already in place. The third electrode (yellow in fig. 4.2) mounts onto the holder, which requires the holder to be made of an insulating material like PEEK. The potential of anode F is defined by the potential of anode B, because it has to be adjusted such that the electron beam leaves the gun parallel to the z axis. This leaves adjustments of the other two electrodes for the optimisation of the focusing properties of the gun, as shown in fig. 4.2.

4.3   Layout

The layout of the gun posed several challenges as it is of utmost importance to have the cathode in a region of minimal magnetic field as discussed in section 1.2. Additionally, in an OAG design the stray magnetic field produces an unwanted effect on the electron trajectory through the Lorentz force. Minimising the magnetic field is usually achieved by using a so called *bucking coil* - a solenoid around the electron gun that is used to adjust for the stray magnetic field of the EBIT's main B-field. Without such a coil, the gun has to be positioned in such a way that the cathode is placed in a region of low magnetic field. For the *tt*EBIT, $B = 0\,\mathrm{T}$ at a spot around $10\,\mathrm{mm}$ away from the holder (see fig. 3.1), which means that the gun has to be as close to the trap centre as possible. This severely restricts the maximum possible gun diameter. The gun is therefore assembled using a
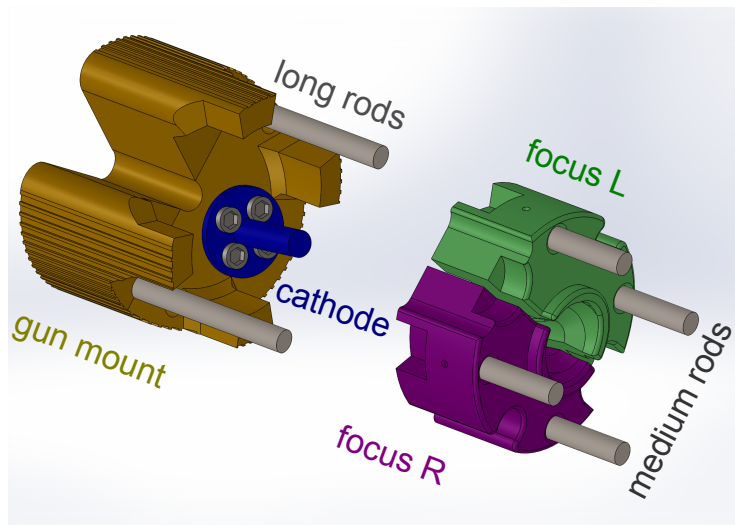
Figure 4.5: First assembly step of the OAG. The gun mount, the rods and the focus electrodes are made of MACOR, ceramics and molybdenum respectively.
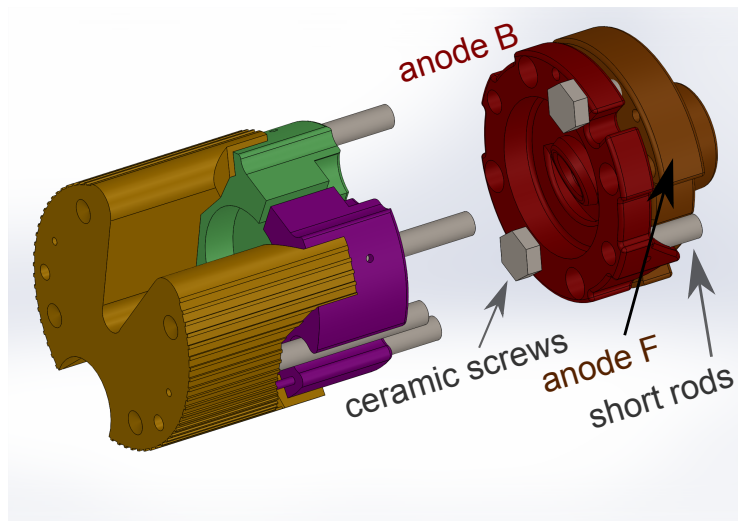
Figure 4.6: Second assembly step of the OAG. The copper anode is held together by ceramic screws.
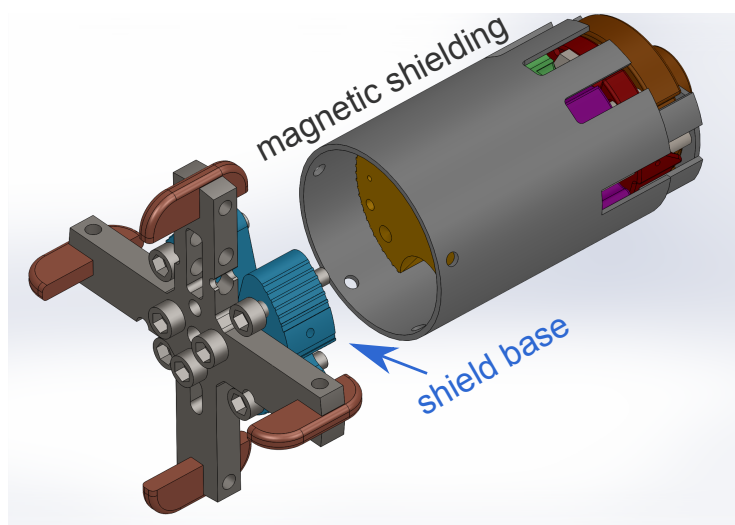
Figure 4.7: Third assembly step of the OAG. The magnetic shielding is made of permalloy.
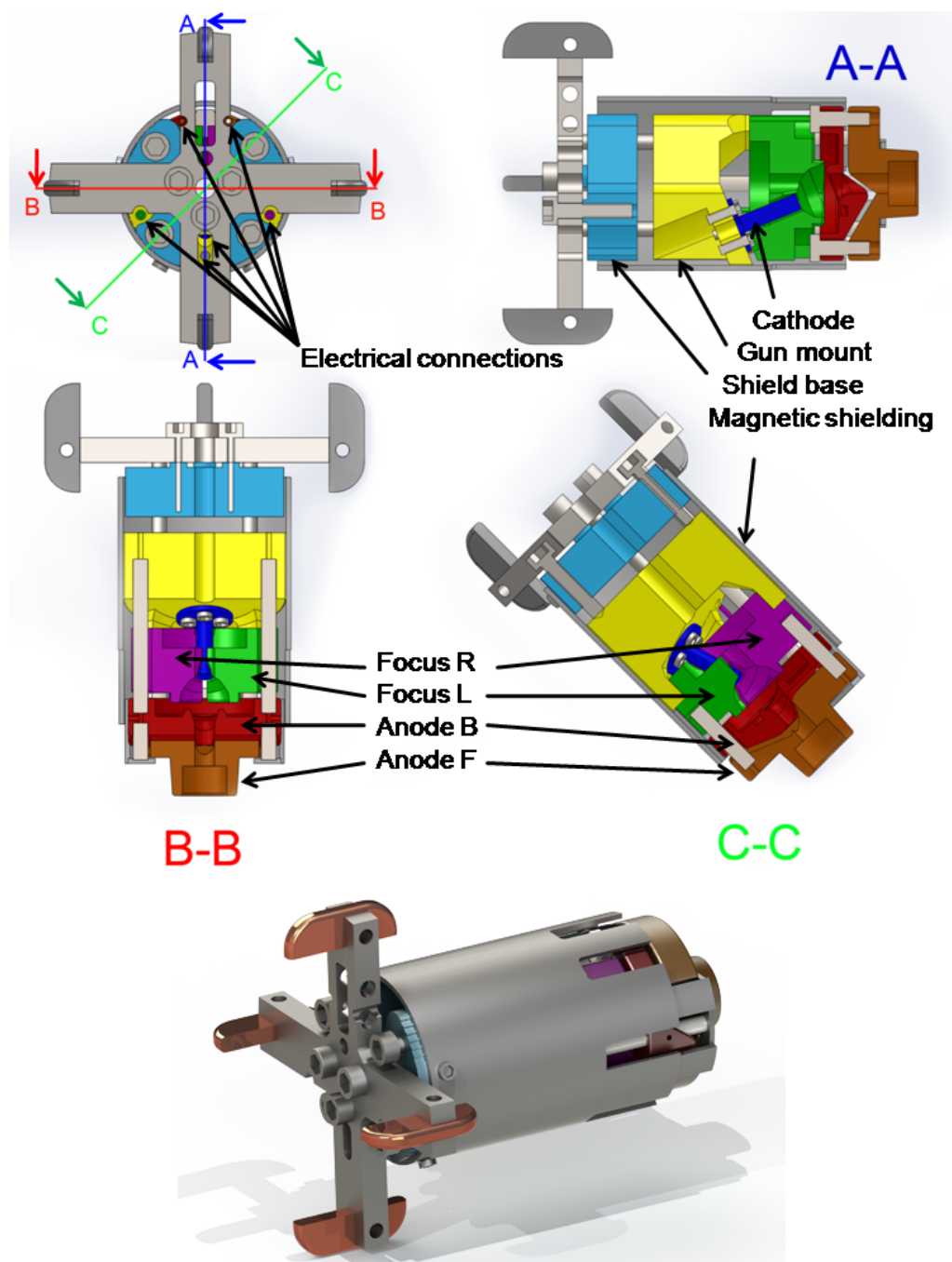
Figure 4.8: Overview of the OAG design: back view (top left), side cutaway view (A-A)(top right), top cutaway view (B-B)(bottom left), and diagonal cutaway view (C-C)(bottom right). The back view shows the electrical connections, while the electrodes can be seen in the cutaway views. The electrodes are: cathode (blue), focus L (green), focus R (purple), anode B (red), and anode F (brown).
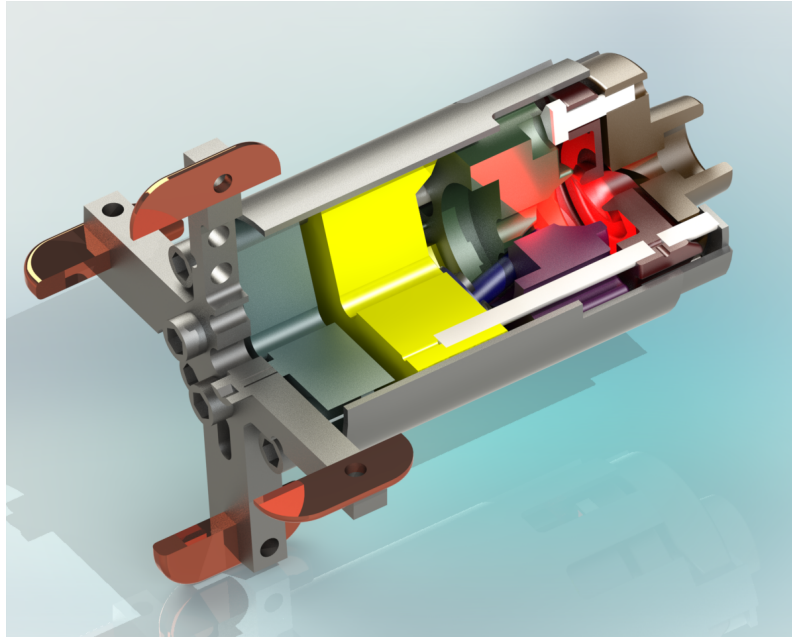
Figure 4.9: Assembled OAG. The electrodes are: cathode (blue), focus L (green), focus R (purple), anode B (red), and anode F (brown).

stacking system which has no need of any screws at the front of the gun (see fig. 4.8 and fig. 4.9). This also has the advantage of allowing for a magnetically shielding cylinder, which further reduces the magnetic field at the cathode position.

An important consideration in the design of the stacking system is the emergence of creeping currents running over the surface of insulating materials like ceramics. Depending on the surface cleanliness they lower the breakdown voltages of the insulators. It is therefore not possible to just stack the electrodes on top of each other using insulating spacers, so a different approach has to be taken. The assembly of the OAG can be summarised in five steps:

1. After installing the cathode, the focus electrodes can be mounted on the gun mount (see fig. 4.5). The gun mount is made of MACOR while the focus electrodes are made of molybdenum due to its high melting point.

2. Anode F and anode B (both made of OFHC copper) have to be held together using two ceramic screws (see fig. 4.6). The distance between them should be greater than 2 mm.

3. After having put four medium length ceramic rods into the focus electrodes (see fig. 4.6), the anode can be mounted onto the gun mount using two long ceramic rods (fig. 4.6). The two screws in the anode can then be tightened such that anode F sits on the four medium length rods.

4. The electrodes are then to be put into magnetic shielding using two short ceramic rods as spacers (see fig. 4.7). The magnetic shielding should not touch any electrodes.

5. The shield base can now be installed by inserting it into the magnetic shielding and fixing it in place. Four screws put through threaded holes inside the base are used to push the gun mount forward, fixing the entire structure in place.

Utilizing the shield base in such a way as opposed to just mounting the gun mount on the magnetic shielding is advantageous because it allows for minor deviations in the construction of the gun; i.e. the electrodes do not have to fit exactly. The electrical connections to the different electrodes are made with metal rods that screw into them. The dedicated holes can be seen in fig. 4.8.

4.4   Simulations

After completion of the design, the beam characteristics were simulated in the range of energies intended for operation. Fig. 4.10 shows electron trajectories obtained for the following electron energies: 56 keV, 5.6 keV, 0.56 keV, and 0.1 keV. The electrode potentials could possibly be further optimised to perfect the beam transport. The effects of a non-zero cathode temperature were not taken into account in these simulations.

The parameters used are listed in table 4.1. The influence of the Lorentz force gets stronger at lower electron energies, which can be seen as a larger voltage between focus L (U_{focL}) and focus R (U_{focR}) relative to the cathode potential.

Table 4.1: Parameters used for the simulations in fig. 4.10. Simulation results are given in the last two columns.

Energy /keV	U_{cat} /kV	U_{focL} /kV	U_{focR} /kV	U_{anB} /kV	U_{anF} /kV	focus $\varnothing_m$ /mm	focus $\varnothing_s$ /mm
56	-36	-34.8	-35.2	20	2.5	0.16±0.02	0.28±0.03
5.6	-3.6	-3.45	-3.55	2	0.25	0.28±0.03	0.57±0.04
0.56	-0.36	-0.33	-0.37	0.2	0.0	1.0±0.1	1.9±0.2
0.1	0.0	0.025	0.0	0.1	0.065	3.5±0.4	3.3±0.4

Table 4.1 also lists the meridional and sagittal diameter of the electron beam at its focus point (focus $\varnothing_m$ and focus $\varnothing_s$ respectively). The simulations show that the focus of the beam is not perfectly round and that the focus diameter increases at lower energies, which increases electron losses.

Nevertheless, it is shown that it is possible to operate the gun even at energies as low as 100 electronvolt, keeping beam losses at only a fraction of the total current. Simulations show that stable operation is possible over a wide range of acceleration voltages (0.1-56 keV). This complex task of off-axis electron extraction inside a magnetic field was achieved with the carefully optimised electrode geometries presented in this chapter.
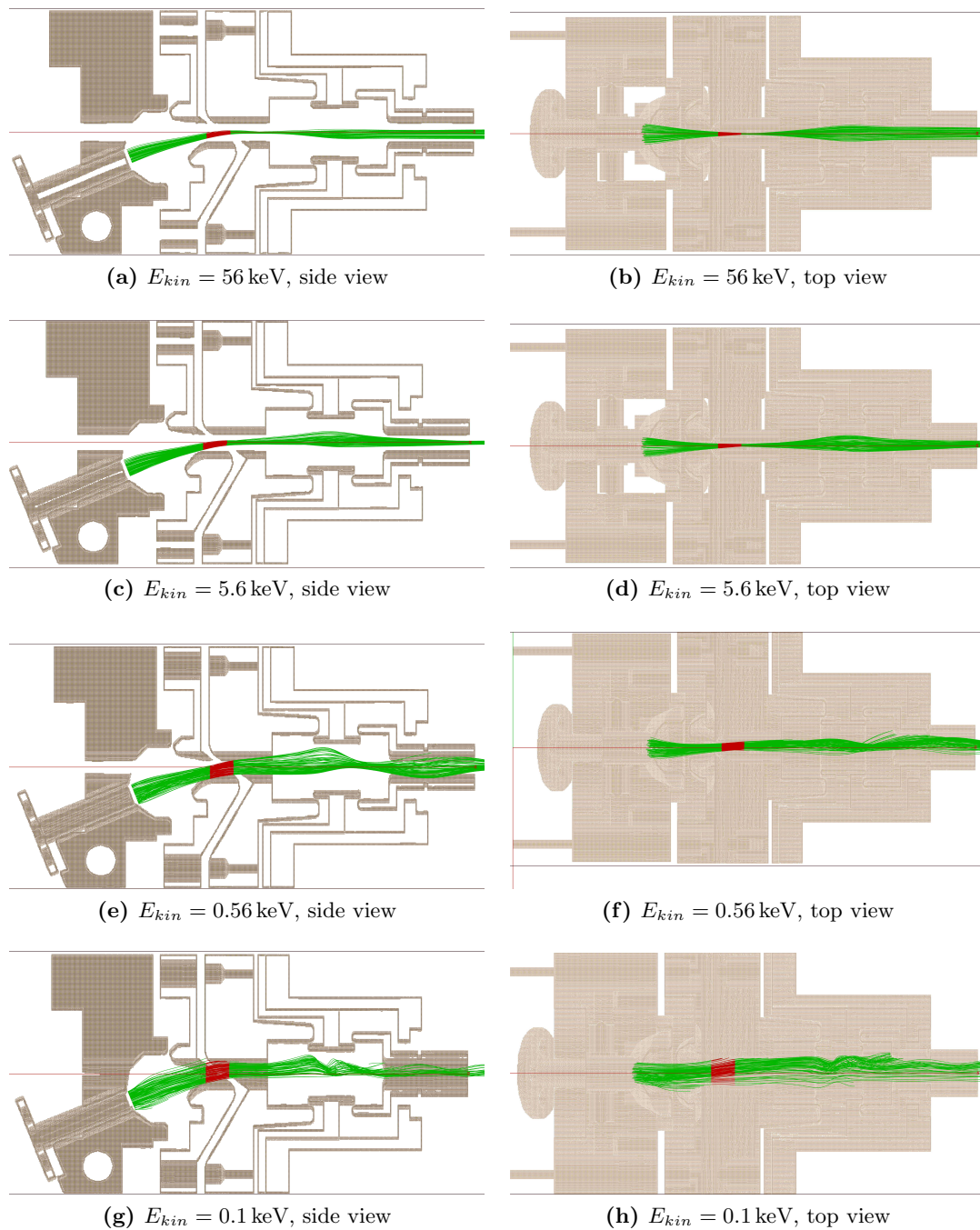
(a) $E_{kin} = 56$ keV, side view

(b) $E_{kin} = 56$ keV, top view

(c) $E_{kin} = 5.6$ keV, side view

(d) $E_{kin} = 5.6$ keV, top view

(e) $E_{kin} = 0.56$ keV, side view

(f) $E_{kin} = 0.56$ keV, top view

(g) $E_{kin} = 0.1$ keV, side view

(h) $E_{kin} = 0.1$ keV, top view

Figure 4.10: Electron extraction simulations made with SIMION. The simulations were made at different at different electron energies which is derived from the voltage between cathode and anode.

Chapter 5

Conclusions and Outlook

A new portable electron beam ion trap (EBIT) called *table-top* EBIT (*tt*EBIT) has been taken into operation for the first time. Different parts for the *tt*EBIT were designed and commissioned, among them the so-called collector electrode as well as an electron gun.

During commissioning using a test cathode, it was found that electron beam spreads out too early, causing the electrons to hit the last drift tube of the trapping assembly. It could be shown however, that under certain conditions this astray current can be kept at a fairly low value. An electron beam current of up to $2.3\,\mathrm{mA}$ passing through the trap was measured. It was found that this value was mainly limited by the quality of the test cathode used for commissioning. Therefore, it is expected that much higher currents will be achieved when a new cathode is installed.

Furthermore, a novel off-axis electron gun (OAG) was designed which leaves the main trap axis free of obstructions. This enables coaxial superposition of a photon beam and the electron beam, maximising the overlap between them, and therefore optimises the photoionisation or photoexcitation rate of the trapped ions.

For its use in an EBIT, an unique electrode design had to be developed. This includes splitting the focus electrode in half to be able to compensate for the Lorentz force due to the stray magnetic field, as well as placing a diagonal cut through the anode which allows for control of the electron beam exit angle. Simulations show that this design can operate in a wide range of electron beam acceleration voltages. The gun components were under construction at the time of writing.

With both the on-axis and off-axis gun, the *tt*EBIT can be used perform spectroscopy on moderately charged ions, for example on Ir^{17+}, which only requires electron energies of $410\,\mathrm{eV}$ for ionisation[29] and is of particular interest in the search for a possible time variation of the fine-structure constant[5].

Appendix A

Appendix: Description of work completed

During the course of my project I worked on the commissioning and testing of the *tt*-EBIT. This EBIT was originally designed by L. F. Buchauer who constructed the magnetic system as well as the main vacuum chamber and the drift tubes including their mounting. The installation of the drift tubes was incomplete however.

Furthermore, I designed and assembled a mounting system for the on-axis electron gun and tested the gun's functionality using the software package TriComp. Further design work included the safety boxes for the feedthrough connectors and an aluminium base plate that could hold and support the entire construction. I also made the necessary schematic drawings which I gave to the mechanical workshop, so they could construct the parts. Lastly, I designed the OAG, including its mounting and parts of a manipulation system.

Parallel to the design of the OAG, I investigated its functionality using the software package SIMION 8.0 and adjusted its geometry accordingly. This took 19 iterations starting from a design inspired by [26]. Some important insights were the right positioning of the cathode as well as the importance of having a split focus electrode to counteract the Lorentz force acting on the electron beam, because this is the first time that an off-axis electron gun is intended to be used inside a magnetic field. Further notable results are the small size of the gun despite the additional electrodes, which was achieved by designing the compact stacking system as well as by bending the electron beam inside the anode (which is also a novel approach to the problem).

Further work of mine was concerned with the heating up of the cathode and installation of the power supplies, leading to the first electron beam. The programme and hardware for reading out the pressure was created by S. Bernitt. I also investigated the electron beam behaviour with emphasis on where the electrons hit, since only a fraction of the emitted beam is detected at the collector.

Appendix B

Appendix: Mechanical Designs

Parts that were designed within the context of this project are shown here in more detail.

B.1 Off-Axis Gun
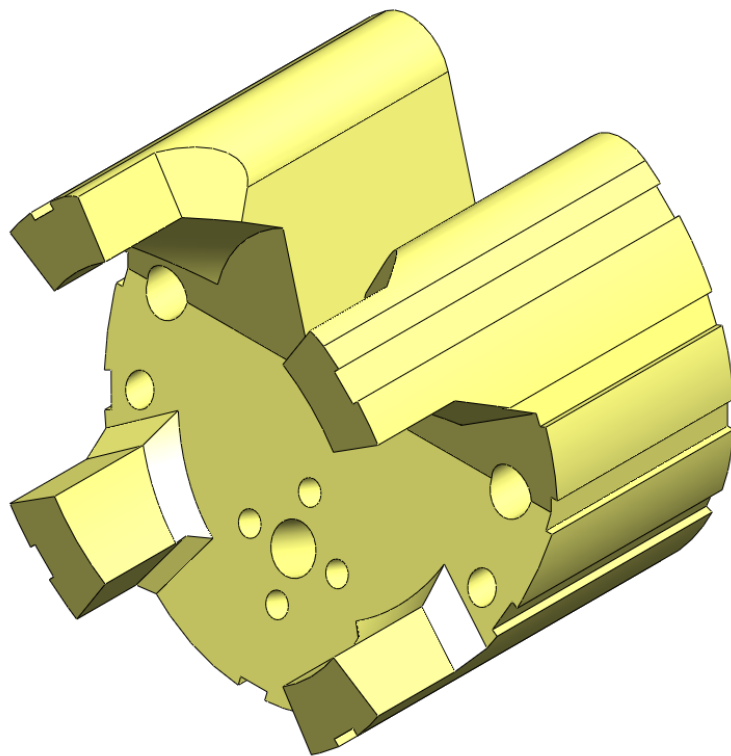
Figure B.1: Insulating gun mount, which holds the focus electrodes and fixes the cathode at an angle of 22°. It has an outer diameter of 33 mm.
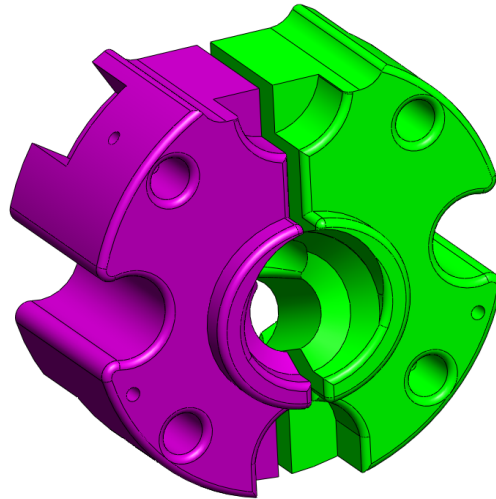
(a)
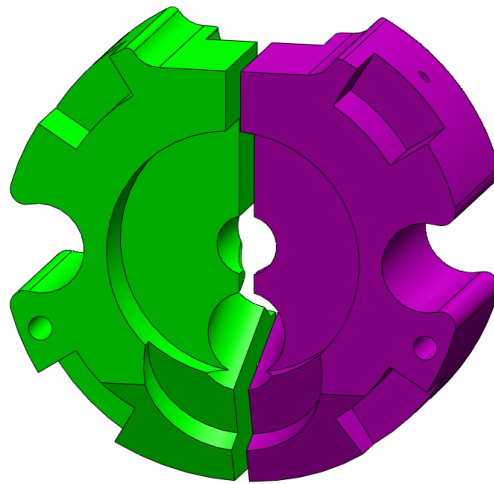
(b)

Figure B.2: Focus L (green) and focus R (purple). The focus electrode is split up in two, to counteract the lorentz force which would push the electron beam to the side. They have an outer diameter of 31 mm.
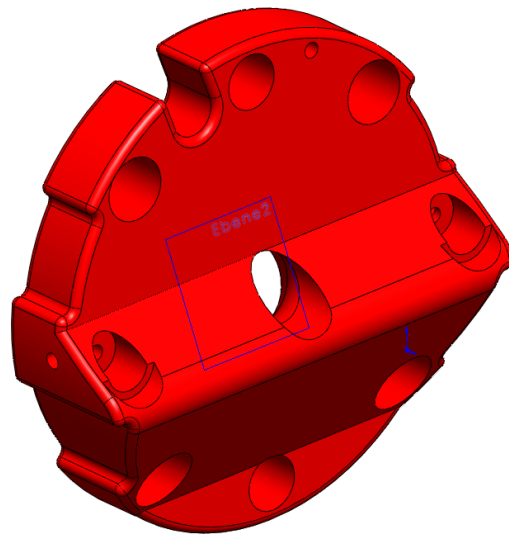
(a)
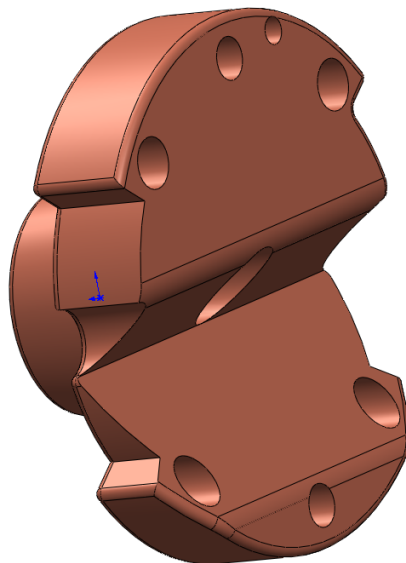
(b)

Figure B.3: Anode B (a), which is responsible for electron extraction from the cathode and anode F (b), which can bend the beam such that it is parallel to the z axis. They have an outer diameter of 31 mm.
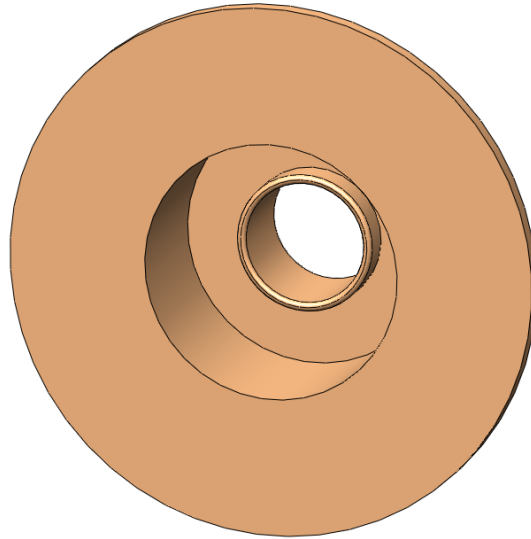
Figure B.4: Electrostatic lens, which is to be mounted between electron gun and drift tubes. It can focus the electron beam and has an outer diameter of 31 mm.
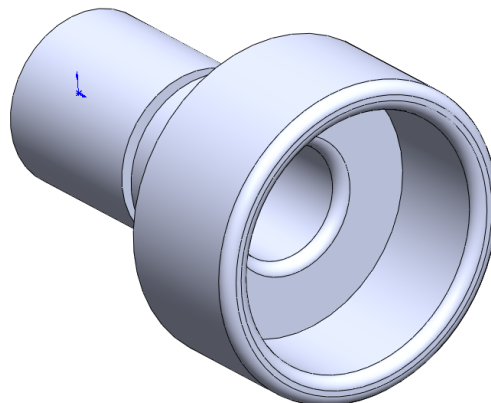
Figure B.5: Modified DT1, to improve the electrostatic lensing with the lens from fig. B.4. It has an outer diameter of 11 mm.
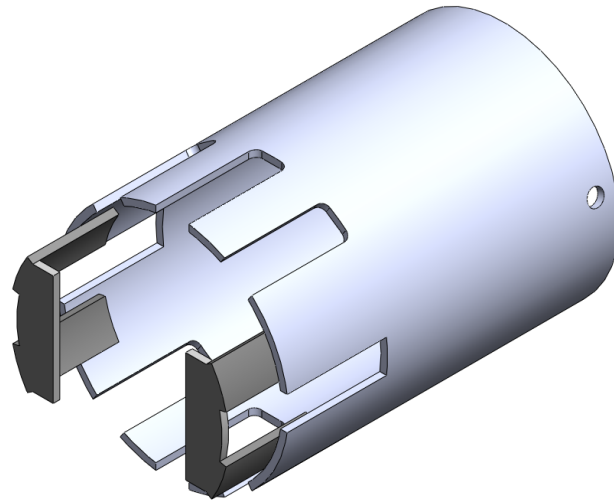
Figure B.6: Magnetic shielding, made of permalloy (light blue) and non-magnetic steel (black). The recesses improve the vacuum. It has an outer diameter of 35 mm.
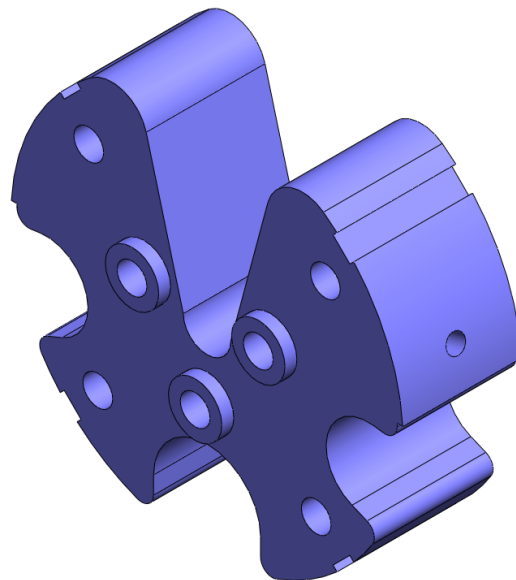
Figure B.7: Shield base used to fix the electron gun in place. It has an outer diameter of 33 mm.
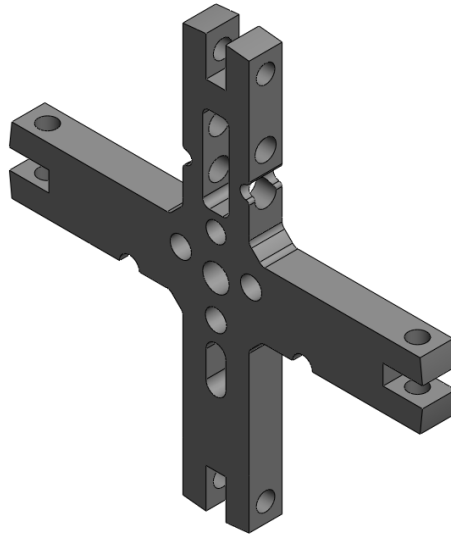
Figure B.8: Adapter piece that connects the electron gun to the manipulator and keeps it concentric using the sledge pieces (fig. B.9). It has an outer diameter of 62.5 mm.
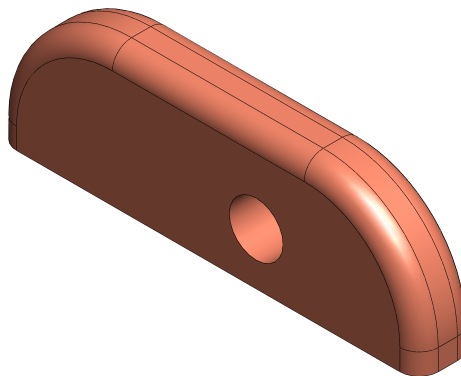
Figure B.9: Copper sledge piece, responsible for keeping the electron gun concentric.

B.2   Collector
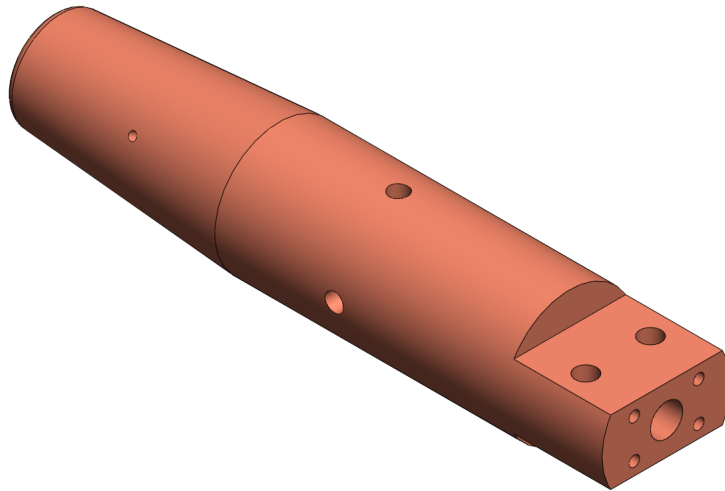
Figure B.10: Collector responsible for absorbing the electron beam. It has a length of 190 mm
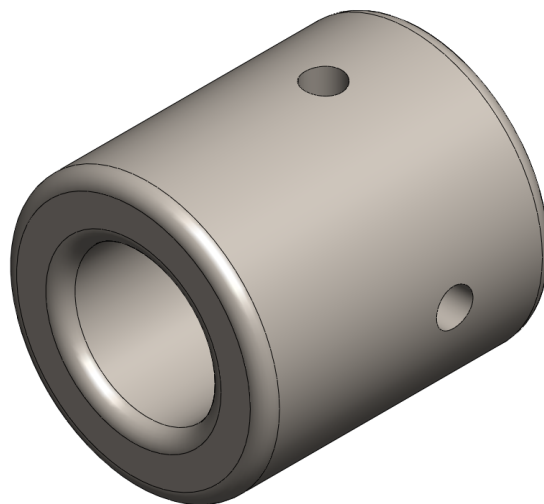
Figure B.11: Extractor electrode, which is meant to facilitate ion extraction and stop electrons from getting through the collector. It has an outer diameter of 18 mm

B.3 Support
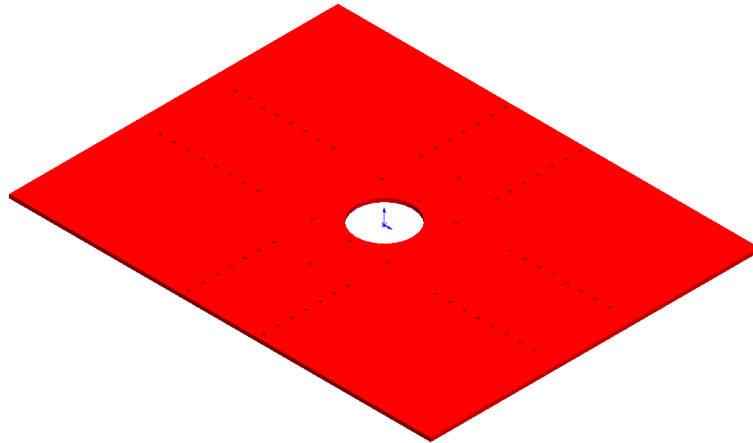
Figure B.12: Plate on which the *tt*EBIT is mounted. Its dimensions are $901\,\text{mm} \times 703\,\text{mm} \times 8\,\text{mm}$ with a hole in the middle with a diameter of $120\,\text{mm}$ which allows access to the *tt*EBIT from below.
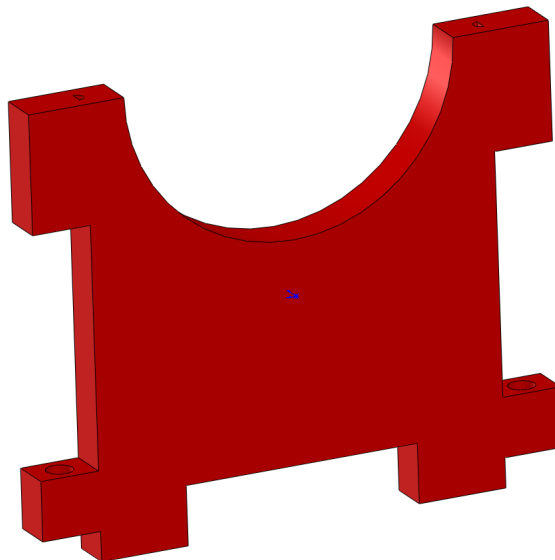
Figure B.13: Vacuum seal support for flanges of with a diameter of $113.5\,\text{mm}$.
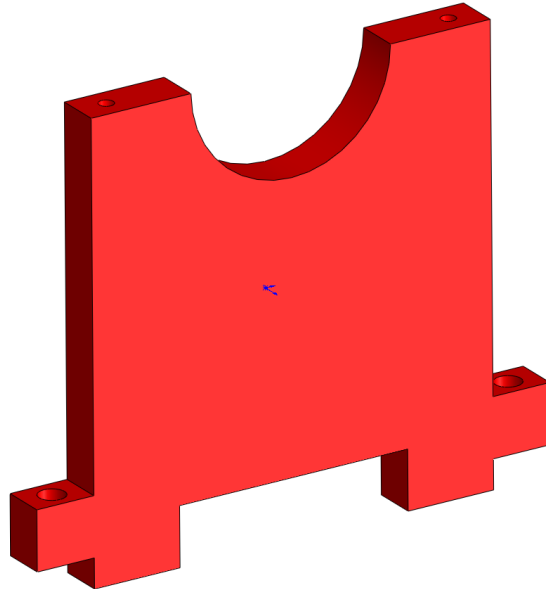
Figure B.14: Vacuum seal support for flanges of with a diameter of 69.5 mm.
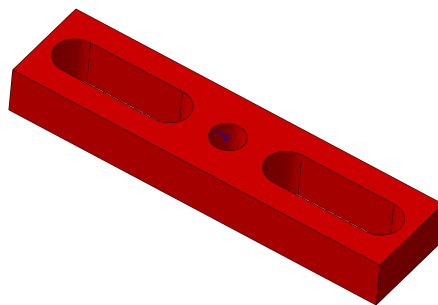
Figure B.15: Vacuum seal support foot, for variable positioning of the support pieces (fig. B.13 and fig. B.14) on the plate.
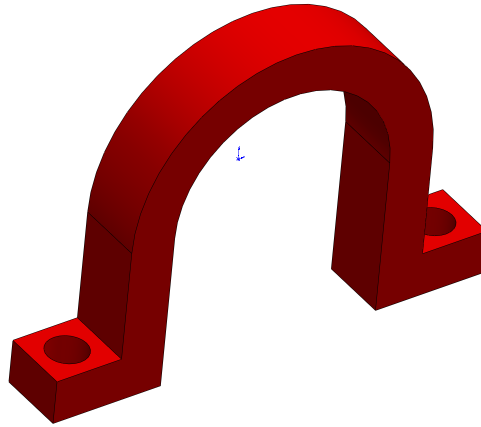
Figure B.16: Aluminium clamp to fix the *tt*EBIT in place.
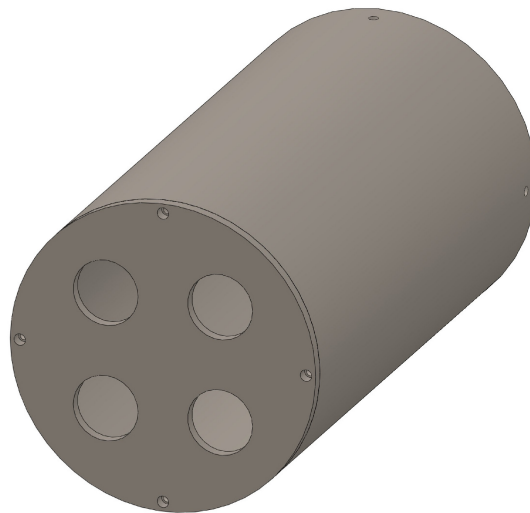
Figure B.17: Safety cover, which attaches to CF40 flanges to protect up to four ceramic feedthroughs.
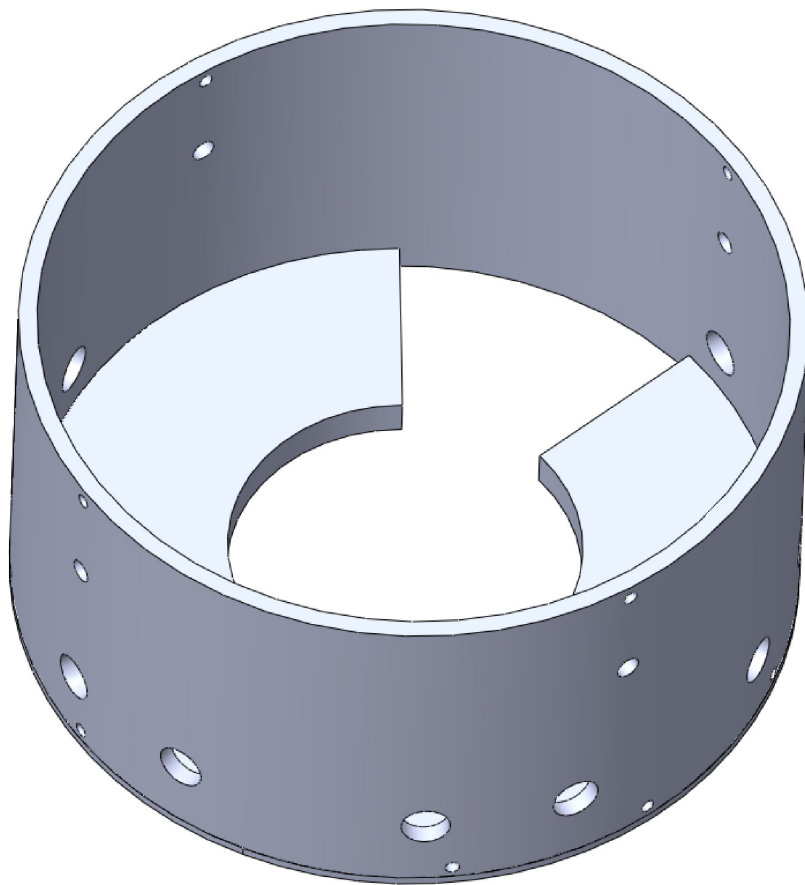
Figure B.18: Large safety cylinder, which attaches to the drift tube feedthroughs for radial access to the connections.
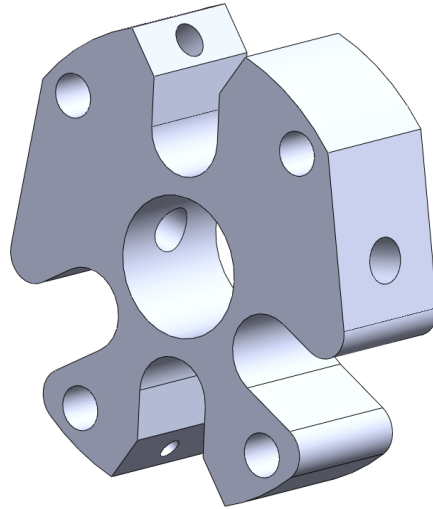
B.4 Gun Mounting

Figure B.19: Holder that connects the on-axis electron gun to a flange. It has an outer diameter of 34 mm.
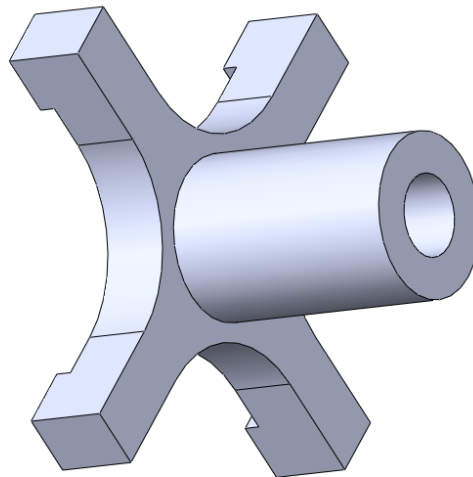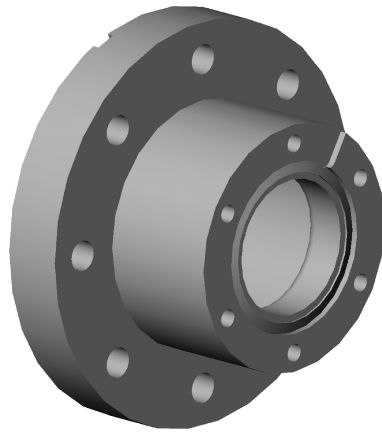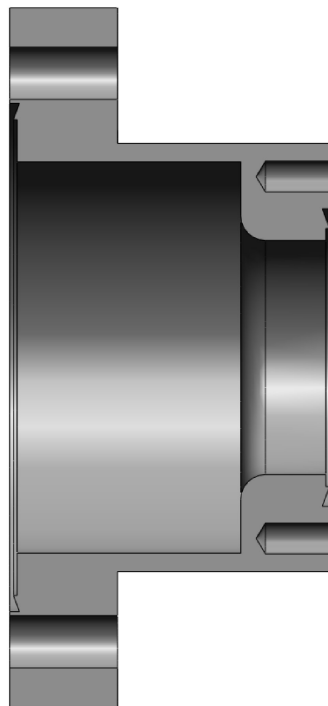

Figure B.20: Holder base, which is welded to a flange while leaving space for four feedthroughs.
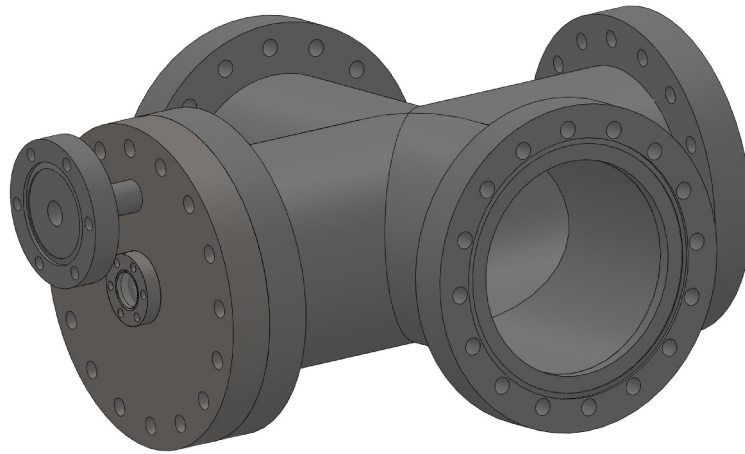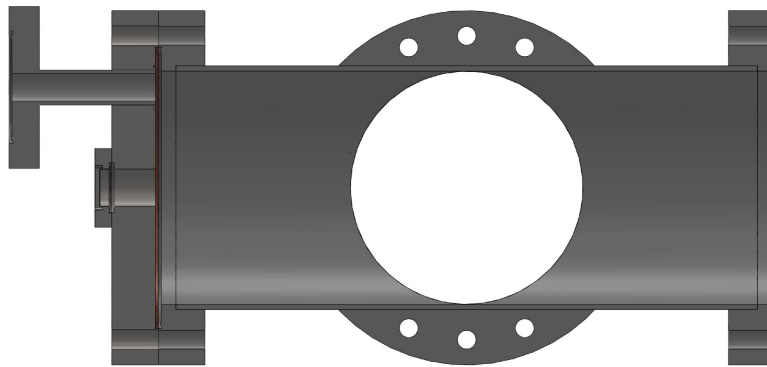
(a)

(b)

Figure B.21: CF63 to CF40 adapter piece for the mounting of the electron gun onto the vacuum chamber that allows for more leeway when manipulating the gun.

(a)

(b)

Figure B.22: Vacuum chamber, which is to attach to the off-axis gun's manipulation system, while still allowing for free access for a laser.

Bibliography

[1] G. Kirchoff. *Kirchoff, über die Fraunhofer'schen Linien.* Polytechnisches Journal , 32 (1860).

[2] W. Grotian. *Zur Frage der Deutung der Linien im Spektrum der Sonnenkorona.* Naturwissenschaften , 214 (1939).

[3] T. Fang & C. R. Canizares. *Probing cosmology with the x-ray forest.* The Astrophysical Journal **539(2)**, 532 (2000).

[4] M. Gargaud, R. Amils, J. Cernicharo Quintanilla, H.J. Cleaves, W.M. Irvine, D. Pinti & M. Viso. *Encyclopedia of Astrobiology.* Springer (2011).

[5] J. C. Berengut, V. A. Dzuba, V. V. Flambaum & A. Ong. *Electron-Hole Transitions in Multiply Charged Ions for Precision Laser Spectroscopy and Searching for Variations in α.* Phys. Rev. Lett. **106**, 210802 (May 2011).

[6] J. K. Rudolph. *Dissertation to be published.* Ruprecht-Karls-Universität Heidelberg (2013).

[7] V. Mäckel, R. Klawitter, G. Brenner, J. R. Crespo López-Urrutia & J. Ullrich. *Laser Spectroscopy on Forbidden Transitions in Trapped Highly Charged Ar^{13+} Ions.* Phys. Rev. Lett. **107**, 143002 (Sep 2011).

[8] S. W. Epp. *Röntgen-Laserspektroskopie hochgeladener Ionen in einer EBIT am Freie-Elektronen-Laser FLASH.* PhD thesis Ruprecht-Karls-Universität Heidelberg (2007).

[9] T.Baumann. *Spektroskopische Untersuchungen resonanter Rekombinationsprozesse an hochgeladenem Silizium in einer EBIT.* PhD thesis Ruprecht-Karls-Universität Heidelberg (2012).

[10] L.F. Buchauer. *Konstruktion einer kompakten Elektronenstrahl-Ionenfalle mit Permanentmagneten für Floureszenzmessungen.* Bachelor's thesis, Ruprecht-Karls-Universität Heidelberg (2012).

[11] Wolfgang Lotz. *Electron-impact ionization cross-sections and ionization rate coefficients for atoms and ions from hydrogen to calcium.* Zeitschrift für Physik A Hadrons and Nuclei **216(3)**, 241–247 (1968).

[12] Heinrich F. Beyer & Viateheslav P. Shevelko. *Introduction to the Physics of Highly Charged Ions (Series in Atomic Molecular Physics) (Vol. 3).* Taylor & Francis (2003).

[13] *TB-128 Notes on Dispenser and Oxide Cathodes.* Heat Wave Labs, Inc. 195 Aviation Way Suite 100, Watsonvielle CA 95076-2069, USA (1999).

[14] S. Humphries. *Charged Particle Beams.* John Wiley and Sons (1990).

[15] J. Orloff. *Handbook of Charged Particle Optics (2nd ed.).* CRC Press (2008).

[16] J. R. Pierce. *Theory and Design of Electron Beams.* Van Nostrana Books Co. (1934).

[17] *Tutorial: high-flux electron gun reference desgin.* Field Precision PO Box 13595, Albuquerque, New Mexico 87192, USA (2010).

[18] G. Herrmann. *Optical Theory of Thermal Velocity Effects in Cylindrical Electron Beams.* Journal of Applied Physics , 127 (1958).

[19] K. Widmann. *High-Resolution Spectroscopc Diagnostics of Very High-Temperature Plasmas in the Hard X-ray Regime.* PhD thesis Technische Universität Graz (1998).

[20] S. Humphries. *Field Solutions on Computers.* CRC Press (1997).

[21] *Trak 6.0 - Finite-element Charged-particle Optics, Electron and Ion Gun Design.* Field Precision PO Box 13595, Albuquerque, New Mexico 87192, USA (2002).

[22] A.J.G. Martínez. *Quantum interference in the dielectronic recombination of heavy highlycharged ions.* PhD thesis Ruprecht-Karls-Universität Heidelberg (2005).

[23] *TB-147 Processing of Dispenser Cathodes .* Heat Wave Labs, Inc. 195 Aviation Way Suite 100, Watsonvielle CA 95076-2069, USA (2004).

[24] S.Bernitt. *Resonante Anregung astrophysikalischer Röntgen-Übergänge in hochgeladenen Eisenionen mit dem Freie-Elektronen-Laser LCLS.* PhD thesis Ruprecht-Karls-Universität Heidelberg (2013).

[25] V. Mäckel. *Laserspektroskopie hochgeladener Ionen an der Heidelberger Electronstrahl-Ionenfalle.* PhD thesis Ruprecht-Karls-Universität Heidelberg (2010).

[26] Y. A. Kubayshin, A. V. Aloev, V. I. Shvedunov & N.I. Pakhomov. *A Novel Electron Gun for Off-Axis Beam Injection.* Particle Accelerator Conference Proceedings. New York, NY, USA (2011).

[27] *Specifications for Magnetic Shielding Foil.* Less EMF inc. 776B Watervliet Shaker Rd, Latham NY 12110, USA (retrieved 31.05.2013).

[28] *TB-176 Custom Dispenser Cathodes with Mounting Flanges.* Heat Wave Labs, Inc. 195 Aviation Way Suite 100, Watsonvielle CA 95076-2069, USA (1999).

[29] J.Scofield. *Ionization Energies.* LLNL inernal report. Livermore CA 94550, USA.